State and Prospects of Wind Hazard Mitigation Research in TPU

Yukio Tamura [a], Masahiro Matsui [a], Akihito Yoshida [a]

[a] *Wind Engineering Research Center, Tokyo Polytechnic University, 1583 Iiyama Atsugi Kanagawa, 243-0297, Japan*

ABSTRACT: In the Global COE Program "New Frontier of Education and Research in Wind Engineering", the objective of the project-1 is to study how to mitigate the wind hazard. To accomplish this objective, following items were investigated, (1) characteristics gust such as tornadoes and thunderstorm, (2) monitoring of response of buildings and structures with GPS, (3) development of experimental system for cladding under wind pressures, (4) wind damage recognition using satellite and aerial images, (5) aerodynamics for various structures and group of buildings, (6) development of engineering virtual organization, EVO, in the cyber-infrastructures and (7) any other issues related to wind engineering in the structural engineering field. These project items were carried out as planned. More researches were carried out additionally. This report shows the outline of the activities and results of the researches.

KEYWORDS: Wind Hazard Mitigation, Wind Resistant Design, Aero Dynamic Database

1 INTRODUCTION

The overarching objective is to develop a gateway of knowledge base aimed at improving the understanding of wind loads and their effects and their efficient modeling at laboratory scale and on computational platforms to achieve robust and cost effective wind-resistant design for urban disaster prevention. The main target areas in wind disaster prevention and mitigation are: to develop rapidly deployable wind observation systems aimed at improving understanding of the wind field characteristics in extreme wind events; to establish robust damage identification schemes at the urban level using satellite imagery and aerial photography; to understand and model the effects of gust events including tornadoes on structures; to develop advanced testing procedures for building exteriors/cladding and components for windborne debris impact and repeated cyclic loadings under buffeting; to enhance understanding and modeling of the aerodynamic characteristics of buildings situated in complex urban environments; to improve the wind resistance of green roofing systems and thermal insulation of roofs for environmental protection and energy savings; to establish a web-based network of GPS monitoring systems to enhance urban disaster prevention; to develop wind-resistant construction methods including retrofit and repair for Asia-Pacific countries and beyond. Other targets areas include: establishment of VORTEX-Winds EVO involving a host of analysis and design modules and knowledge bases; to develop domain knowledge necessary for populating the EVO and its maintenance.

2 CHARACTERISTICS OF TORNADO-LIKE FLOW AND ITS EFFECT TO BUILDINGS, DISASTER INVESTIGATION, DAMAGE RECOGNITION FROM AERIAL IMAGES

2.1 Experimental Research

Tornado is very rare but one of the severest wind event for most countries. In Japan, around 20 to 40 tornadoes have been observed annually. Tornado events are characterized by unpredictability, short life span and danger, making real time evaluation difficult. This necessitates analysis of tornado-wind loadings on buildings in laboratory situations. With this objective, scaled building models were subjected to a stationary vortex created using a tornado simulator. Parameters that govern a tornado like flow such as swirl ratio, aspect ratio were in close agreement with previous studies. In the present investigation the influence of factors such as building location relative to vortex center, swirl ratio, and terrain roughness on the mean and peak pressures in a building model under tornado-like flow is evaluated. Building faces perpendicular to the tangential flow experiences lesser suction pressures compared to the other faces near the core boundary, whereas they experience higher suction pressures far from vortex center. Lower swirl ratios produce higher roof suction pressures compared to building walls whereas higher swirl ratios have roof suction comparable with pressures on leading edge wall. The effect of roughness was to enhance suction pressures on roofs of buildings and decrease the pressure magnitudes on side walls compared to a near smooth ground.

Post tornado damage investigations revealed building roof and openings on buildings as two critical failure modes. The effect of building location relative to vortex, terrain roughness and swirl ratio on measured internal pressures for two opening ratios namely 3.9% and 0.1% on buildings were determined. Higher negative minimum peak internal pressure coefficients are experienced by a 3.9% opening ratio case within vortex core compared to case of 0.1%. This behavior reverses outside the vortex core. Lowest minimum net peak roof force coefficients can increase to four fold, for the same building location but different building orientation.

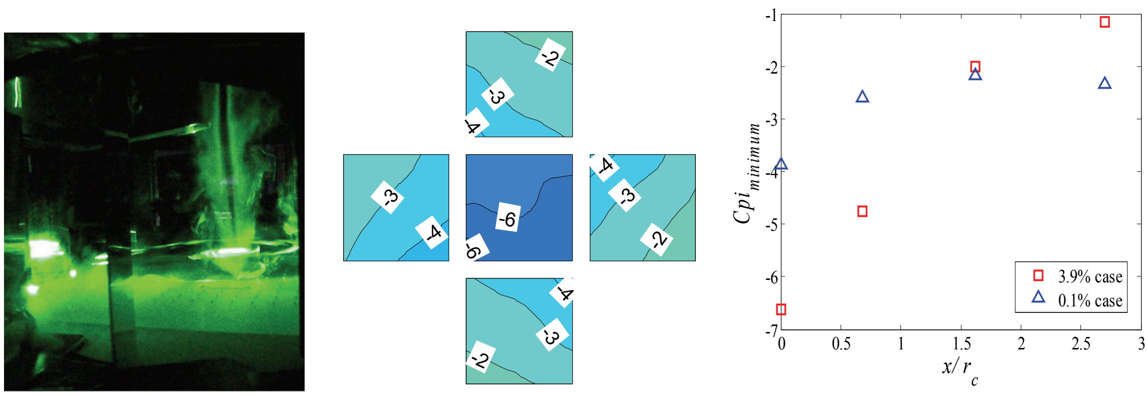

(a) (b) (c)

Fig.1 (a) Tornado vortex visualized in the simulator (b) Mean pressure coefficients on cube faces (c) Minimum peak internal pressures at different building locations for two opening ratios [1]

2.2 Site investigation after tornado disaster

Based on JMA data, 124 gusty winds are observed on the Japanese islands in 2009 and 2010. Of the total, 63 were tornadoes, 11 were downbursts, 9 were gust fronts, 21 were water spouts, and 20 were unknown phenomena. As an example, the major tornadoes, gust fronts and downbursts in 2009 are shown in Fig.2.

Damage investigations, including, Tsukuba-tornado on May 6th 2012 in Tsukuba, Ibaraki, Japan, were carried out actively by GCOE members. As the one of the resolutions for sharing resources, EVO (Engineering Virtual Organization [https://www.vortex-winds.org/]) was developed and released in 2010. The damage database is one of the main contents of EVO. The Browsing interface of the damage database in Vortex-Winds is shown in Figure 13. When each point is clicked, the browsing interface for each structure appears as shown in Figure 14. The damage database, powered by Google Earth, allows users to geographically view submissions of fellow VORTEX-Winds members, sorting by location, event classification and damage attributes. Registered members can also upload their own damage reports to the database.

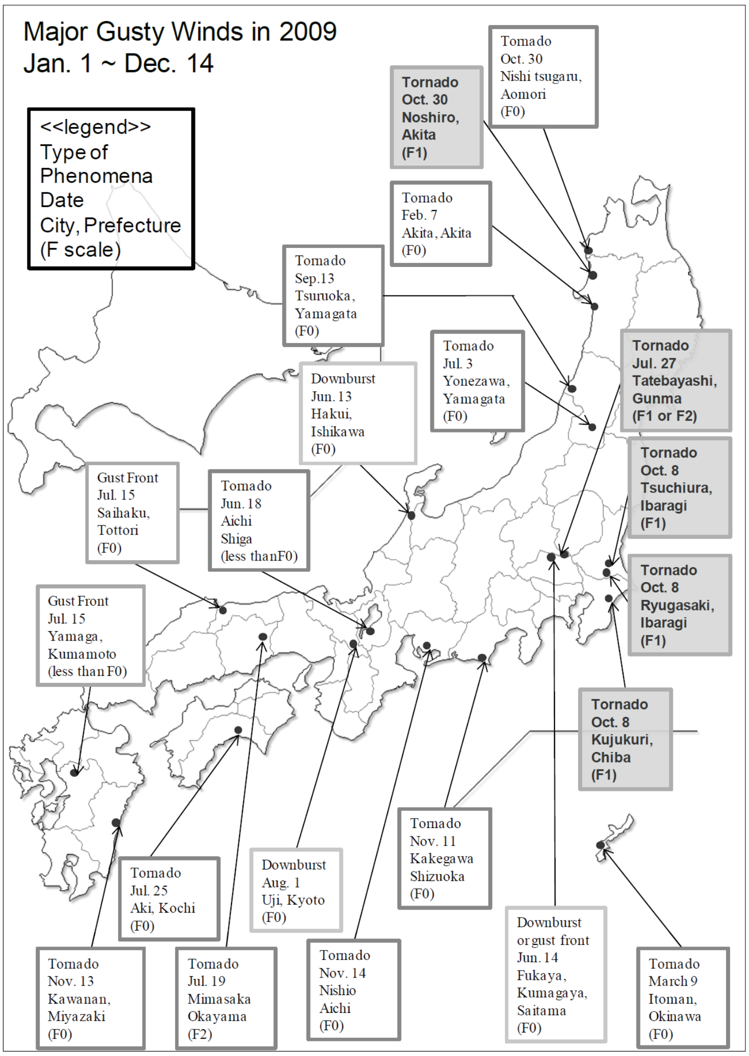

Fig.2: Damages due to the gusty winds in 2009 in Japan [2]

2.3 Automatic wind damage detection from remote sensing image signals using wavelet based pattern recognition

Damages to building structures, due to strong winds, such as tropical cyclones and tornadoes have been a fact of life since time immemorial. Rapid relief provided by recognizing the appropriate damaged locations as well as the buildings will reduce the impact of such disasters and will aid conventional field investigations after a strong wind disaster. Here wind damage location identification is done automatically from low resolution remote sensing imagery, initially by using texture-wavelet analysis on wind borne debris deposits, for a quick survey and for emergency aid. Then the damaged location in the low resolution is mapped on high resolution imagery. From this the buildings are automatically segmented by using color invariance properties and edge detection. Damaged buildings are automatically identified using wavelet based feature extraction, in-hand with artificial neural network, (ANN) and support vector machine (SVM). An economical identification of wind damaged buildings from post-storm imageries alone using texture-wavelet analysis is then performed in the current work. It was observed that even using post-storm alone an accurate damaged building identification could be achieved. Percentage area of roof damage is also quantified using texture-wavelet analysis on change detected damaged building roofs as well as on the post-storm roof images alone. A good positive correlation with manually obtained percentage area of damage was obtained even by using post-storm alone. New user friendly software is designed for rapid and easy damage detection from debris deposit. Application of the current research in real time situations such as that of Tuscaloosa, US tornado and Tokunoshima tornado in Japan and in other type of natural disasters such as Thailand flood, water covered area detection were also investigated. Application in determining F-scale of the tornado from debris deposit path width and a generalization of automatic damaged building detection is also determined in this research. Thus accurate and faster wind damage identification from a remote sensing perspective is successfully achieved through this research.

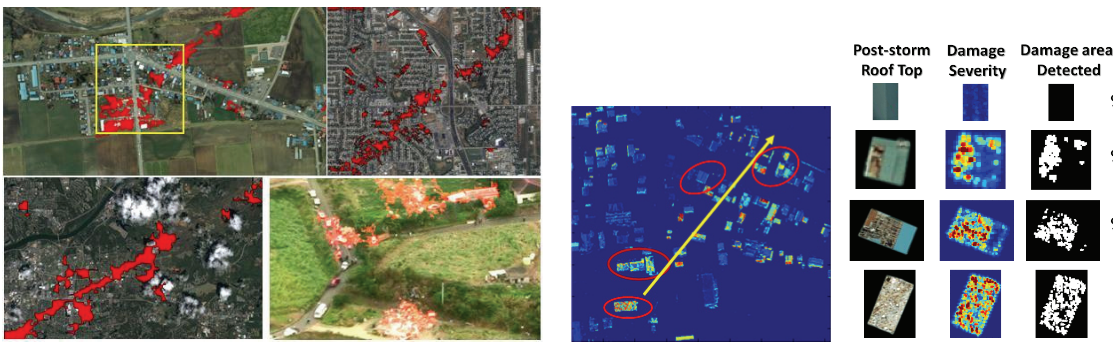

(1) (2) (3)

Fig.3: (1) shows the damaged path detected from debris deposit by texture-wavelet analysis on post-storm imageries alone, once the damage is identified the buildings are segmented at the damaged location and damaged building are identified and shown in (2). (3) shows the percentage area of damage identified automatically. [3]

3 ESTABLISHEMENT OF WIND-INDUCED RESPONSE MONITORING NETWORK FOR BUILDINGS USING GPS TECHNOLOGY

3.1 Objective of this research topic

In current wind resistant design, wind loads on buildings and the wind environment around buildings are examined while projects are still in the planning stages, and they are not confirmed after the completion of construction. Surrounding environments have a strong effect on wind loads on buildings, and wind loads on buildings in urban areas are also changing with the growth of cities. Buildings should be treated as elements of an urban area. If publicity of this policy succeeds, it will be possible to realize long-life cities. This will provide good direction from the viewpoint of safety, environment, and economy. In previous researches[4], feasibility studies have been conducted on wind-induced responses of buildings by using RTK-GPS (Real-Time Kinematic GPS) and it was concluded that responses with amplitudes larger than 2.0 cm and natural frequencies lower than 2.0 Hz could be detected by RTK-GPS. However, to obtain responses in urban areas by GPS, there is a difficulty in deciding the location of the reference station. To solve this problem, a virtual reference station is introduced in this paper. The possibility of a virtual reference station was investigated by full scale tests. It was concluded that the virtual reference station can be used as a reference station, and a monitoring network for buildings was established in the Tokyo area.

3.2 Necessity of Virtual Reference Station

In urban areas, it is especially difficult to set reference stations at arbitrary points. To avoid these difficulties, the virtual reference station system is employed. The Virtual Reference Station consists of multiple GPS reference stations, as shown in Fig.4 (at least 3 stations are needed). As multiple GPS reference stations, ‘GEONET: electronic reference points by the Geographical Survey Institute’ or ‘original reference points’ are employed.

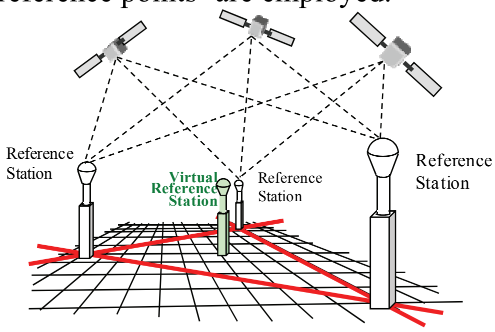

Fig.4 Concept of virtual reference station

3.3 Establishment of real-time-observation network for measuring structural response in urban area

Based on the results showing the measuring capabilities using RTK-GPS shown in the last section, we established a real time observation network in the Tokyo area. In this network, an electric reference is not used for the reference station. We set 3 reference sensors as shown in Fig. 5. The incremental time was 0.1 seconds. The 3 sensors for measuring points were on top of 4 buildings in the center of the Tokyo area. Fig. 6 depicts the elevations of these buildings.

The sampling frequency of recording data was 10 Hz. In the measuring system, the recording data was transferred to the Analysis PC in Tokyo Polytechnic University and the response could be monitored in real time. Fig. 7 shows the power spectrum of the deformation of Build. 1 based on measured data obtained by this GPS system [NS and EW direction]. When strong wind was acting on the building, there was a peak around 0.35 and 0.38Hz. This peak could be found in the record of the accelerometer set at the same location. It was confirmed that these peaks were the natural frequency. Moreover, in this figure, the frequency components in the low frequency range show high values. This means that the average (static) component could be grasped using this GPS system.

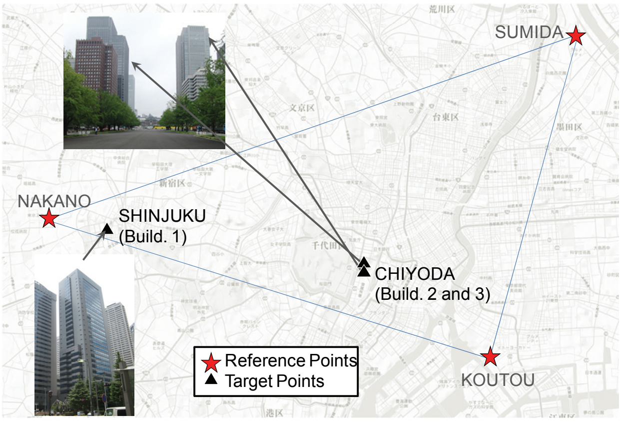

Fig. 5 locations of reference and measuring points

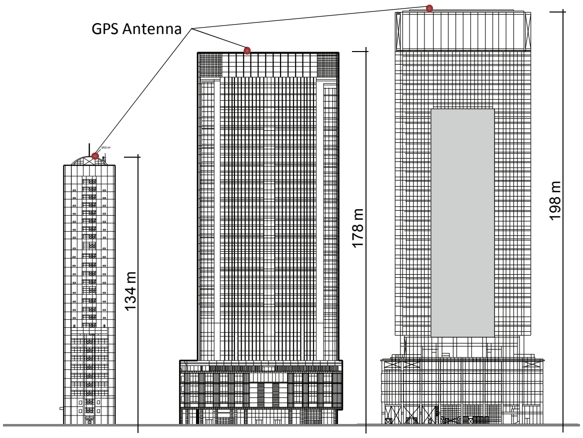

Fig. 6 Elevations of measured building

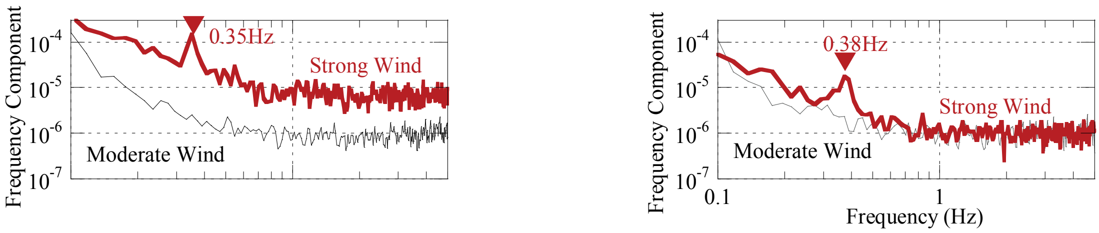

(a) NS direction

(b) EW direction

Fig. 7 Frequency characteristics of measured displacement

4 INVESTIGATION OF WIND RESISTANT PERFORMANCE USING PRESSURE CHAMBER

4.1 Development of wind resistant performance test system

In the past damages due to the strong winds such as tornadoes, typhoon, down burst, most of damages are on the low rise buildings. Especially, damages of cladding, roof panel, ceiling board are remarkable as shown in Fig. 8. The pictures in Fig. 8 show the damages on eaves and ceiling boards. Recently, the peak pressure coefficients are estimated under various types of conditions in the wind engineering field (using wind tunnel tests, numerical simulations, and field measurements) for cladding design and effective-design materials are organized. However, as shown in these pictures, there are many kinds of the details on the ceiling boards, claddings, eave etc. So it is important to establish the testing system to clarify the strength of cladding against the severe suctions under static and dynamic conditions. The experimental system for simulating the behaviors of the cladding [It is called pressure chamber] was set in our Wind

Engineering Research Center. The specimen of the cladding is set on the top face of the pressure chamber and pressure inside the chamber (chamber pressure) can be adjusted from -10kPa to 10kPa. This experimental system consists of 3 parts (Pressure Generating Section, Pressure Adjusting Section, and Test Section). This system is controlled by the personal computer as shown in Fig. 9. In the pressure generating section, there are the 2 fans (11 kW). One of them is for positive pressure supply and another one is for negative pressure supply. In the Pressure Adjusting Section, there is a interlock valve for adjusting the pressure inside the pressure chamber.

Fig. 8 Damages due to the strong wind on the ceiling board and eave

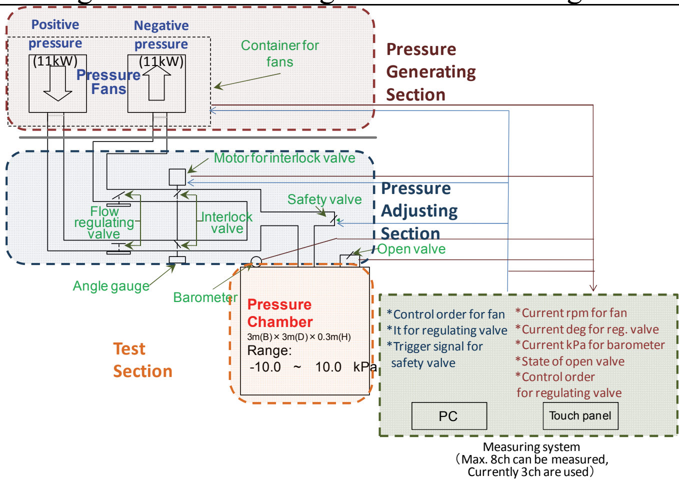

Fig. 9 Conceptual Drawing of experimental system

4.2 Wind resistant performance of a ceiling panel system of piloti

For establishing the experimental method and solving the problems of test using the pressure chamber, the ceiling setup was set as the specimen the pressure chamber and the strength of the specimen was measured.

Fig. 10 shows the Vertical displacement of Ceiling Panel and Ceiling Joist. As shown in this figure, -2.45kPa is the strength of this ceiling system based on the results of this experiment. The main reason of the collapse of this ceiling system is 2 types of the failure of the Screw as shown in Fig 11.

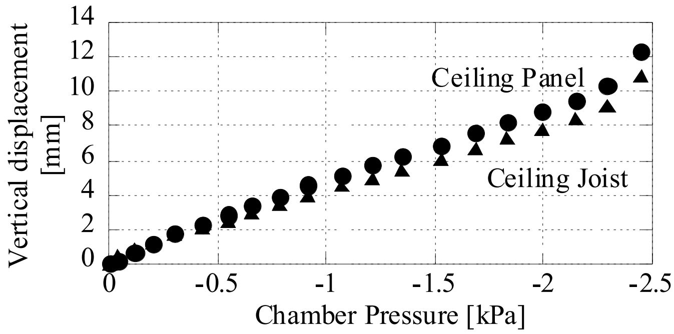

Fig. 10 Vertical displacement of Ceiling Panel and Ceiling Joist

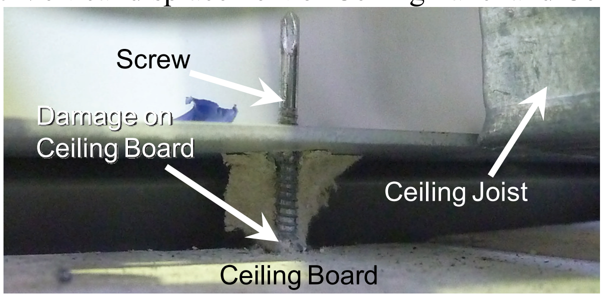

(a) Damage of Ceiling board

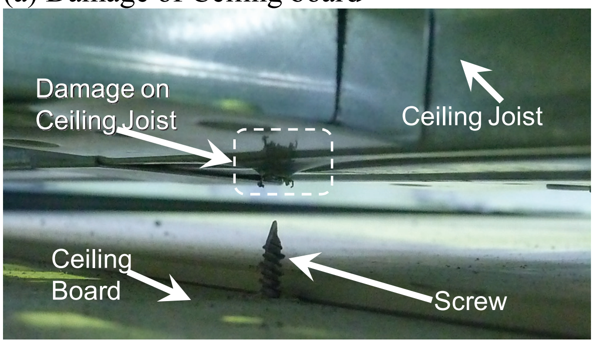

(b) Damage of Ceiling joist

Fig. 11 Observed 2 types of damages on strength test of ceiling system

5 INTERFERENCE EFFECT ON TWO ADJACENT TALL BUILDINGS

5.1 Introduction of this research topic

Most wind load codes have been derived for isolated buildings. However, wind loads on tall buildings surrounded by other tall buildings in real environments may be quite different from those on isolated tall building. Surrounding tall buildings can either increase or decrease not only overall wind loads on a building but also local peak pressures acting on the building cladding. Unfortunately, few codes have referred to wind-induced interference effects on wind loads on buildings (AS/NZS 1170.2[5], 2002; AIJ, 2004[6]). These codes only briefly accommodate wind load effects of neighboring tall buildings, mainly dealing with shielding effects, which is beneficial to the building structural system and claddings. Because there are a large number of variables involved, such as building size and shape, relative locations of interfering building(s), wind

directions, upstream terrain conditions and so on, it is difficult to consider all parameters in codes.
The main aim of this study is to tackle the problem of interference for local peak pressures on a tall building in order to establish a generalized set of guidelines. Extensive wind tunnel experiments have been conducted to measure local peak pressures on a tall building with an interfering building for different height ratios and various wind directions for an urban exposure condition.[7][8]

5.2 Wind tunnel experiments

Wind tunnel experiments on a high-rise building model with various arrangements and height ratios of an adjacent building were carried out in a Boundary Layer Wind Tunnel located at Tokyo Polytechnic University, Japan as shown in Fig 12. For this study, the flow of the atmospheric boundary layer in the wind tunnel was interpreted as a geometrical scale of approximately 1:400. The approach flow represented an urban wind exposure using the spire-roughness technique with a power law exponent of 0.27. The wind speed and the turbulence intensity at the height of the model (principal building) were 8.2 m/s and 20%, respectively.

The considered experimental models comprised two buildings: the pressure model, referred to as the principal building, and the other model, referred to as the interfering building. Fig 13 shows the coordinated system indicating the different locations of the interfering building and wind directions. The center-to-center spacing between them was varied by S_x longitudinally and S_y laterally. Table 1 shows cases of the experimental models used in this study.

The fluctuating wind pressures on the building faces were simultaneously sampled every 0.00128 seconds and the sampling period was 7.5 seconds for each sample. The data were digitally low-pass filtered at 300 Hz. For each test case, 15 samples of 10-min length in full-scale conversion were analyzed. The tubing effects were numerically compensated by the gain and phase-shift characteristics of the pressure measuring system. The pressure data were filtered by means of a moving average filter corresponding to 0.2sec in full scale. Further, the maximum and minimum peak pressure coefficients were calculated by the Cook & Mayne method.

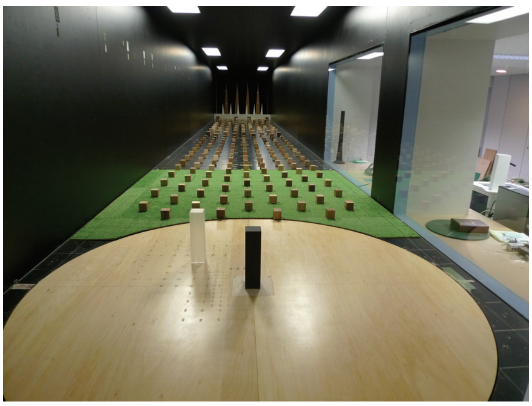

Fig 12: Experimental models in wind tunnel

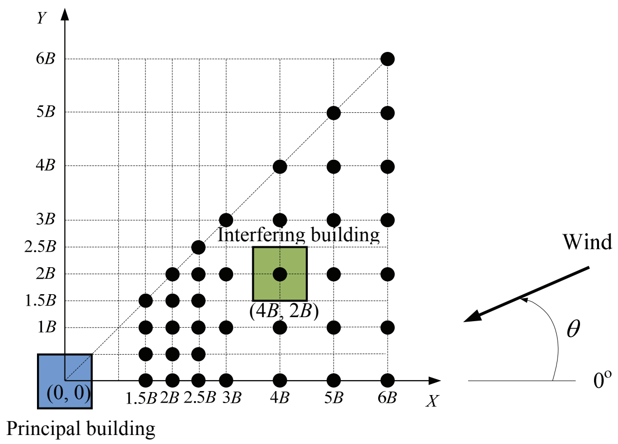

Fig 13: Coordinated system indicating different locations of interfering building and wind directions.

Table 1. Experimental models

Experimental models	Dimensions (mm) (B×D×H)	Height ratios (H_r=H_{ib}/H)	Locations	Wind directions
Principal building	70×70×280	1	1	0^o – 355^o (5^o steps)
Interfering building	70×70×140	0.5	37	0^o – 355^o (5^o steps)
	70×70×196	0.7	4	
	70×70×280	1	37	
	70×70×420	1.5	37	
	70×70×560	2	4	

∗ H and H_{ib} are height of principal building and interfering building, respectively

5.3 *Simultaneous pressure measurement and flow visualization*

To obtain further information and understanding on the interference mechanism for enhanced local peak pressures on the principal building with interfering building of H_r=1, flow fields around two buildings for worst wind directions in tandem and oblique arrangements have been investigated by simultaneous pressure measurements and flow visualization using dynamic particle image velocimetry (DPIV) in wind tunnel of Shimizu Institute of Technology, Japan. This system consisted of a high-speed digital video camera, a double pulse Nd: YAG laser and a particle generator. The fluctuating wind pressures and the image of particle were simultaneously sampled every 0.0001 seconds and the sampling periods were 7.5 seconds and 6 seconds for each sample, respectively. Tracer particles were discharged from downstream of the principal building and then circulated in the wind tunnel. The particles were illuminated by a pulsed laser light sheet. The image was captured in digital memory using a computerized data acquisition system for a field of view of 276mm×207mm.

5.4 *results and discussions*

5.4.1 *Effects of building arrangement*

The minimum negative peak pressure coefficient ($\check{C}_p$) for all measurement points on the principal building and all wind directions can be expressed by:

$$\check{C}_p = \min_{i,j,\theta}\left[\check{C}_p(i,j,\theta)\right] \tag{1}$$

Fig 14 shows the contour of $\check{C}_p$ on the principal building for interfering buildings of different height ratios and various locations, and $\check{C}_p$ on the isolated building was -3.7. From Fig 14, $\check{C}_p$ on the principal building was decreased and expanded with increase in height ratio of the interfering building.

Another interesting observation was that $\check{C}_p$ for H_r=1 and 1.5 significantly decreased when the interfering building was located in oblique arrangement. However, it should be noted that the critical locations of the interfering building vary with increase in height ratio. Interference effects of $\hat{C}_p$ on the principal building were also investigated in this study.

However, the results show that $\hat{C}_p$ on the principal building for interfering building of different height ratios and various locations was similar to that an isolated building.

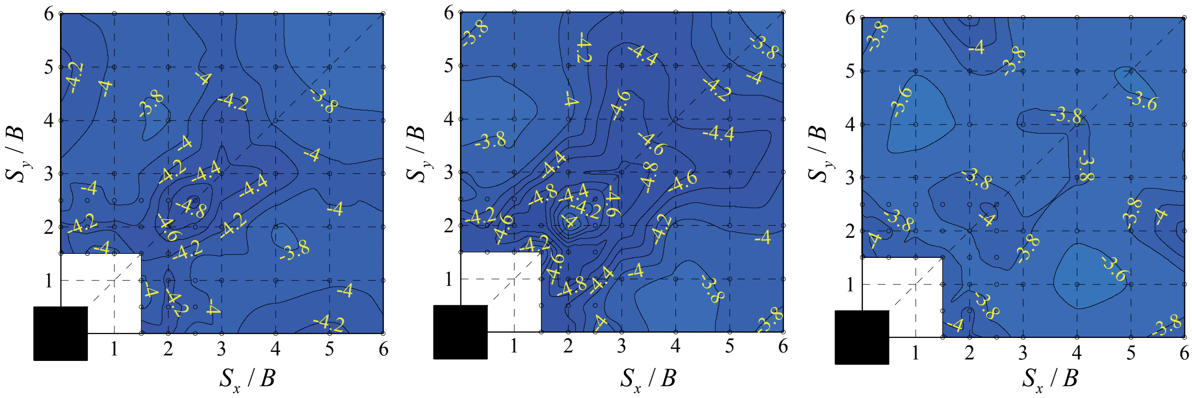

(a) Height ratio (H_r) = 0.5 (b) Height ratio (H_r) = 1 (c) Height ratio (H_r) = 1.5

Fig 14: Contour of $\check{C}_p$ on principal building for interfering building of various height ratios and locations ($\check{C}_p$ (Isolated) = -3.7).

5.5 *Flow pattern in oblique arrangement*

Fig 15 shows the instantaneous pressure coefficients on the principal building with interfering building of H_r=1, velocity vector and vorticity fields around two buildings in oblique arrangement with (S_x,S_y)=(2.5B,2.5B) for wind direction θ=65^o when the smallest minimum peak pressure coefficient on the principal building occurs. From Fig 15(b) and (c), the strong shear layer generated by the interfering building directly hit the principal building, leading to increased momentum at the upper face (front wall) of the principal building. This rose to a high pressure coefficient near the leading edge of the upper face of the principal building, as shown in Fig 15(a). Furthermore, it is inferred that some changes of wind directions (55$^o \leq \theta \leq$ 85^o) could lead to an obvious decrease in minimum peak pressure coefficients acting on the principal building.

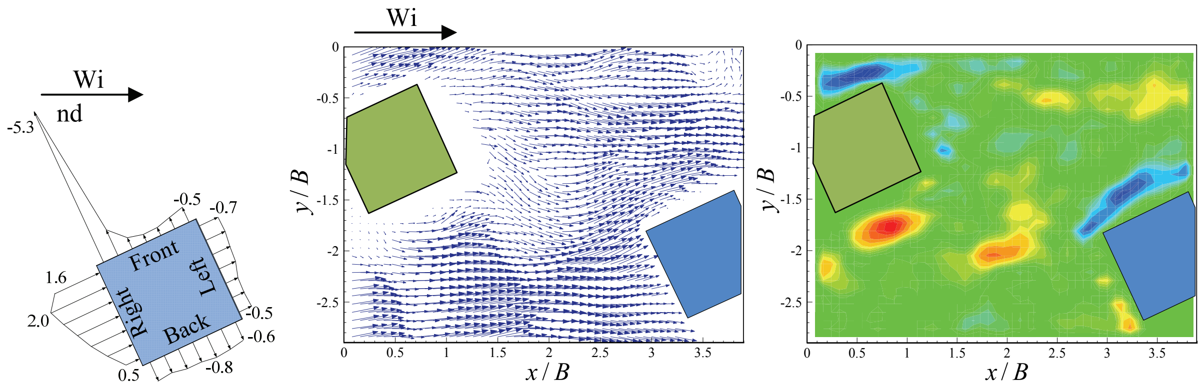

(a) Pressure coefficients (b) Velocity vector field (c) Vorticity field

Fig 15: Instantaneous pressure coefficients on principal building with interfering building of H_r=1, velocity vector and vorticity fields for wind direction θ=65^o in oblique arrangement (Minimum vorticity and increment of vorticity contour are 100 and 100s-1, respectively).

5.6 *Conclusions*

A detailed and comprehensive study of wind-induced interference effects on buildings has been carried out. Based on the results of these detailed experiments that consider various relevant parameters, general guidelines for limiting conditions have been formulated and critical interference effect situations identified.

6 WIND LOADING ON POROUS SUNSHADE ROOF COVER SHEETS

6.1 Introduction of this research

Scaffolding is a temporary structure used to support people and material in the construction or repair of buildings and other large structures. It is usually a modular system of metal pipes or tubes. For safety, environmental and noise considerations, it is commonly net clad or sheet clad. On construction sites, scaffolding collapses sometimes occur due to strong wind when the scaffolding is covered with sheets of 0% porosity, which significantly increases the wind forces acting on it (Katsutoshi Ohdo, 2005). Furthermore, buildings of different structural types have different kinds of wall openings during construction stages, which also significantly affect wind forces (F. Yue, 2005; Yasumichi Hino, et al, 2005). Thus, the influence of building opening ratios should be considered in the design stage when estimating wind forces acting on scaffolding. For different construction sequences and engineering needs, for a common rectangular section building, scaffolding arrangements vary from one side to all four sides, which affect the wind flow between building and scaffolding (Yasumichi Hino, et al, 2005).

In this study, wind tunnel experiments were carried out based on a prototype of scaffolding attached to a medium-height building, and covered with sheets of 0% porosity. A systemic study of the influence of different building openings on wind forces acting on scaffolding covered with sheets was conducted, and scaffolding arrangements were also taken into account.

6.2 Experiment setup

Two scaffolding sheet models 5mm thick and 0.363m high were selected to simulate 0% porosity sheets covering scaffolding, attached to a medium-height building with 1/75 geometric scale.

304 pressure taps were arranged on both outer and inner sides of the two sheet models (Sheet A and Sheet B). 4 building opening ratios and 6 scaffolding arrangements were considered. Building opening ratios ϕ_B for Models B0, B20, B40, B80 were 0%, 20% 40%, 80%, respectively, and two dummy models (no pressure taps) of sheets were used in some scaffolding arrangements. Fig. 16 shows experiment pictures. Fig. 17 shows building models and scaffolding arrangements.

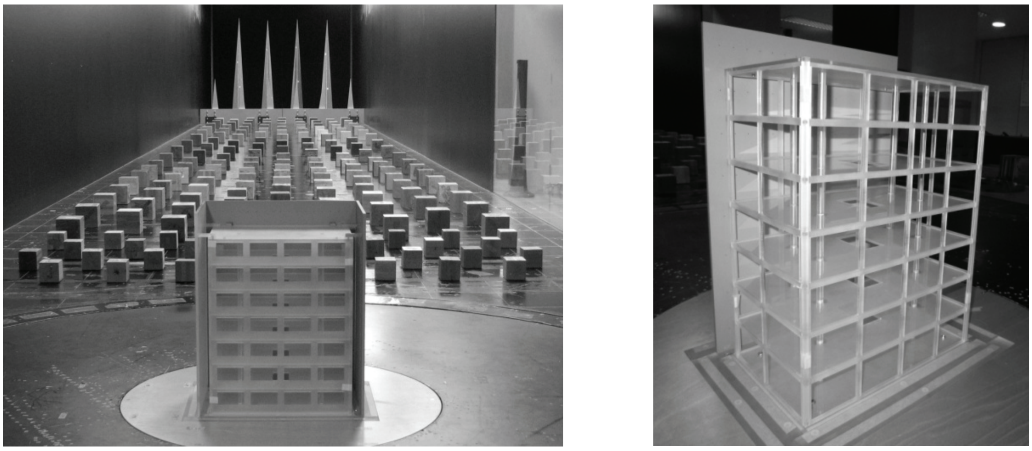

(a) U1 arrangement, ϕ_B =40% (b) I1 arrangement, ϕ_B =80%

Fig.16: Experiment pictures

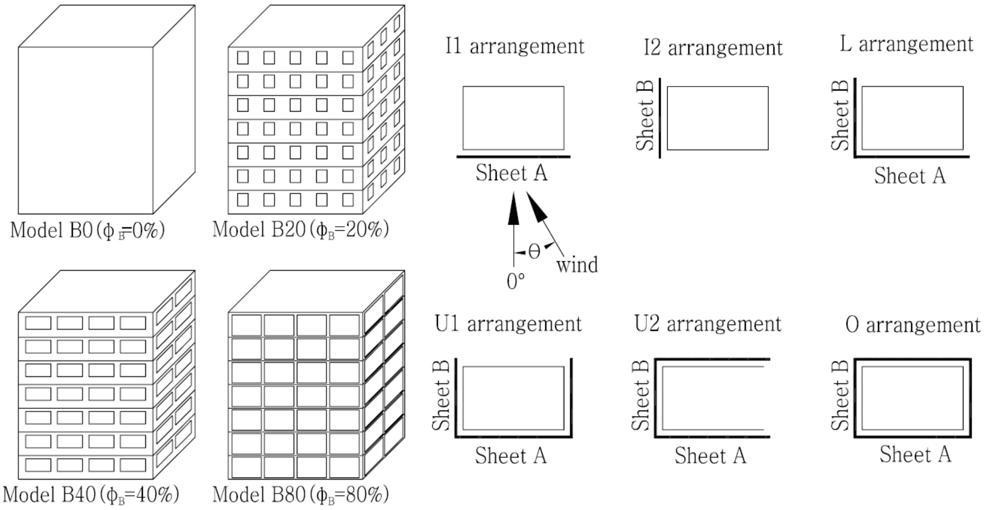

(a) Building models (b) Scaffolding arrangements

Fig. 17: Building models and scaffolding arrangements

6.3 Results and discussions

The maximum local mean C_f usually occurs near wind direction 45 degrees for scaffolding arrangement I1. Fig. 18 shows the local mean C_f distribution of model Sheet A for scaffolding arrangement I1 and wind direction 45 degrees. The maximum local mean C_f occurs at the top corner of the model when ϕ_B (building opening ratio) increases, and the value of the maximum local mean C_f becomes smaller, from 2.6 decreasing to 1.8 at the corner of the model.

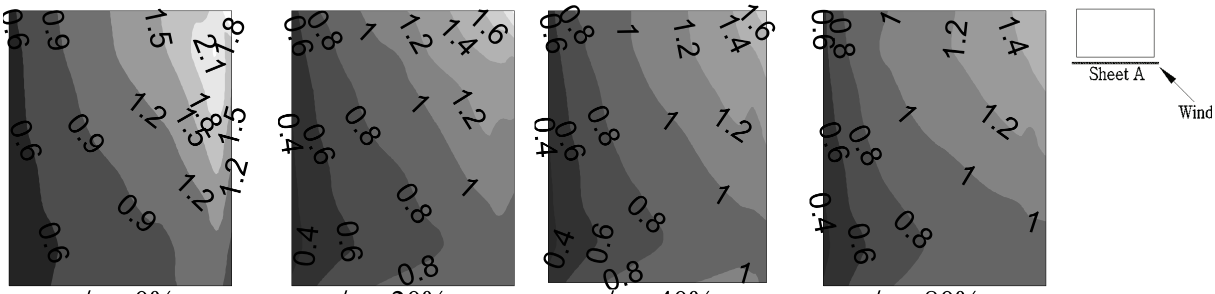

ϕ_B =0% ϕ_B =20% ϕ_B =40% ϕ_B =80%

Fig. 18: Local mean wind force coefficient distribution, arrangement I1, 45 degrees (Sheet A)

The maximum and minimum mean wind force coefficients are expressed as maximum local mean $C_f(i,\theta, \phi_B)$ and minimum local mean $C_f(i,\theta, \phi_B)$, respectively, where i and θ indicate the i-th pressure tap and the approaching wind direction, and ϕ_B is building opening ratio. Fig. 19 compares the maximum local mean $C_f(i,\theta)$ and minimum local mean $C_f(i,\theta)$ of model Sheet A for different building opening ratios. For arrangement I1, when ϕ_B increases from 0% to 80%, the maximum local mean $C_f(i,\theta)$ becomes smaller, changing from 2.6 to 1.8, and the minimum local mean $C_f(i,\theta)$ also becomes smaller, from -1.2 to -1.4. For arrangement L, when ϕ_B increases from 0% to 80%, the maximum local mean $C_f(i,\theta)$ becomes smaller, changing from 2.2 to 1.6, and the minimum local mean $C_f(i,\theta)$ also becomes smaller, from -1.6 to -2.1. For arrangements U1 and U2, the maximum local mean $C_f(i,\theta)$ is almost unchanged, and minimum local mean $C_f(i,\theta)$ changed within the range of ±0.3 for different ϕ_B. For arrangement O, both the maximum local mean $C_f(i,\theta)$ and minimum local mean $C_f(i,\theta)$ are almost unchanged.

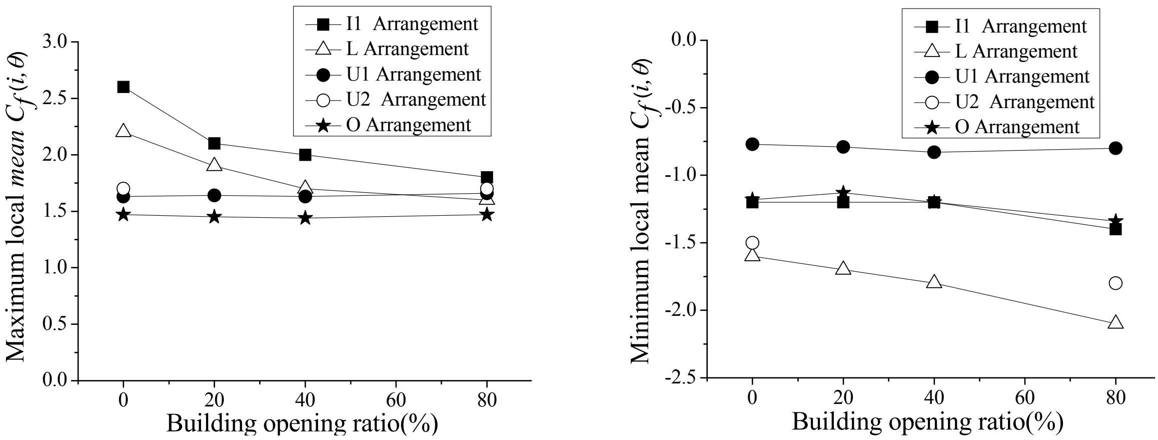

Fig. 19: Maximum local mean $C_f(i,\theta)$ and minimum local mean $C_f(i,\theta)$ for each building opening ratio (Sheet A)

Eurocode imply that the force coefficient for wind loads should be 1.3 for winds normal to the scaffolding and 0.1 for winds parallel to the scaffolding, although BS EN 12811 states that these values should not be used for a completely clad building(H. Irtaza et al., 2012). Chinese code consider the conditions of building with openings and without opening, for sheet clad scaffolding, JGJ 128 (Safety and technical code for frame scaffolding with steel tubules in construction) recommends wind force coefficient should be 1.3φ when building with openings and 1.0φ for no opening, φ is solidity of sheet. SCEA(Scaffolding and Construction Equipment Association of Japan) recommends C_f considering parameters of aspect ratio of scaffolding sheets, subarea and location of sheet, and so on.

Fig. 20 shows the maximum positive total panel $C_f(\theta, \phi_B)$ for each scaffolding arrangement. When scaffolding arrangement is I1, I2, U2 and O, the maximum total panel $C_f(\theta, \phi_B)$ from wind tunnel experiment, 1.41, exceed 1.3 which BS EN 12811 and JGJ 128 recommend, but lower than 1.61 which was calculated from SCEA Recommendations.

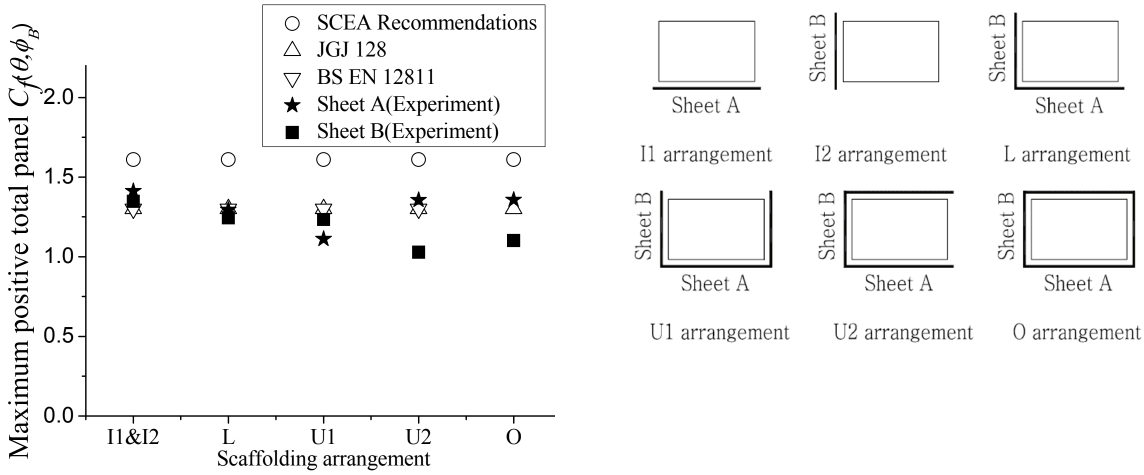

Fig. 20: Comparison between experimental results and wind load recommendations

7 WIND LOADING ON POROUS SUNSHADE ROOF COVER SHEETS

7.1 Introduction of this research topic

Thermal reduction is always a problem for building roofing systems, especially folded steel sheet systems. Roof insulation helps reduce space heating and cooling, thus reducing requirements for heating and cooling system capacities, increasing occupant comfort, and even eliminating condensation on roof surfaces in cold climates. Several roof insulation systems have been used up to now, including the loose laid paver system and heat insulating roof tiles. However, these systems are still expensive. Porous sunshade roof cover sheets have been introduced as a cheaper alternative. This solution has several advantages, including cheapness, quick installation and applicability to both new and existing roofs (see Fig. 21 for this solution). Porous sunshade roof cover sheets installed on folded steel sheet systems reflect sunlight, thus reducing the amount of sunlight reaching the roof. The air layer between the sheet and the roof prevents the thermal conduction. Fig. 22 illustrates some applications of porous sunshade roof cover sheets to a real roof of a low-rise building.

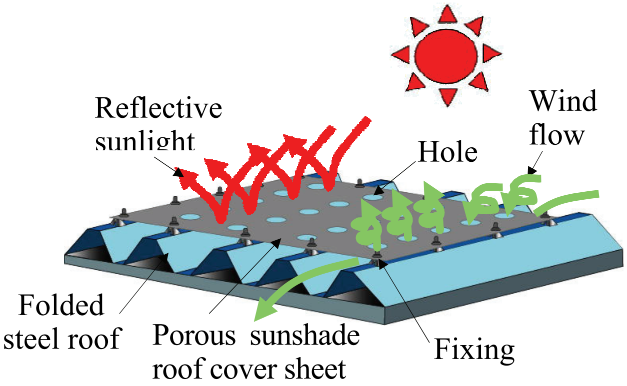

Fig 21: Sketch of porous sunshade roof cover sheet for a building roof

Fig 22: Porous sunshade roof cover sheets on a real building

7.2 Wind pressure experiments[9]

The wind tunnel experiments for a low-rise building model with the porous sunshade roof cover sheets were carried out in a Boundary Layer Wind Tunnel, located in Tokyo Polytechnic University, Japan. The test section in the wind tunnel has 2.2 m wide by 1.8 m high cross-section. For this study, the flow of atmosphere boundary layer in the wind tunnel was interpreted as a geometrical scale of 1:50. Terrain category III (profile exponent of 0.2) in AIJ-RLB (2004) was chosen for the experiments, corresponding to suburban terrain.

The tested model at a length scale of 1:50 is 200 mm high (H) × 470 mm wide (B) × 710 mm deep (D), as shown in Fig. 23. The prototype dimensions of the low-rise building were thus 10 m high × 23.5 m wide × 35.5 m deep. There were 3 test model cases to consider the effect of porosities (ratio between area of orifices and area of the sheet) of the porous sunshade roof cover sheets (0%, 5% and 10%) with gap between the sheet and the profiled roof a = 4.7 mm (see Fig. 23).

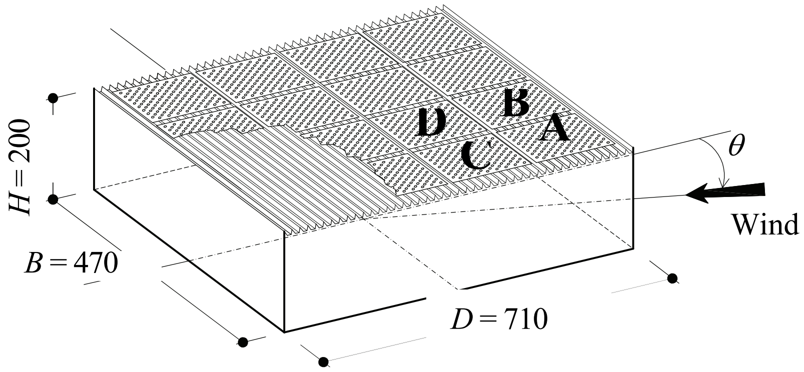

Fig 23: Test model

7.3 Propose of conversion factor

Fig. 24 shows variations of the largest maximum peak and smallest minimum peak panel wind force coefficients $\hat{C}_F$ and $\check{C}_F$ for sheets A, B, C and D with different porosities ϕ. Generally, the absolute values of the largest $\hat{C}_F$ and the smallest $\check{C}_F$ decreased as the porosity increased. The differences between the largest $\hat{C}_F$ for sheets A and D and for sheets B and C at porosity ϕ=

0% and 10% were very small. The same phenomenon occurred for values of $\check{C}_F$ for porosity ϕ= 10%. The largest values of $\hat{C}_F$ for porosity ϕ = 0% and 5% were higher than that for porosity ϕ = 10% up to 180% and 57%, respectively. These values for $\check{C}_F$ were 176% and 45%.

Based on the results of wind pressure experiment, conversion factors γ_L^{ϕ} to evaluate the wind load acting on the porous sunshade roof cover sheet for porosity ϕ and an underneath volume ratio V^* = 0.018 are given inFig. 25.

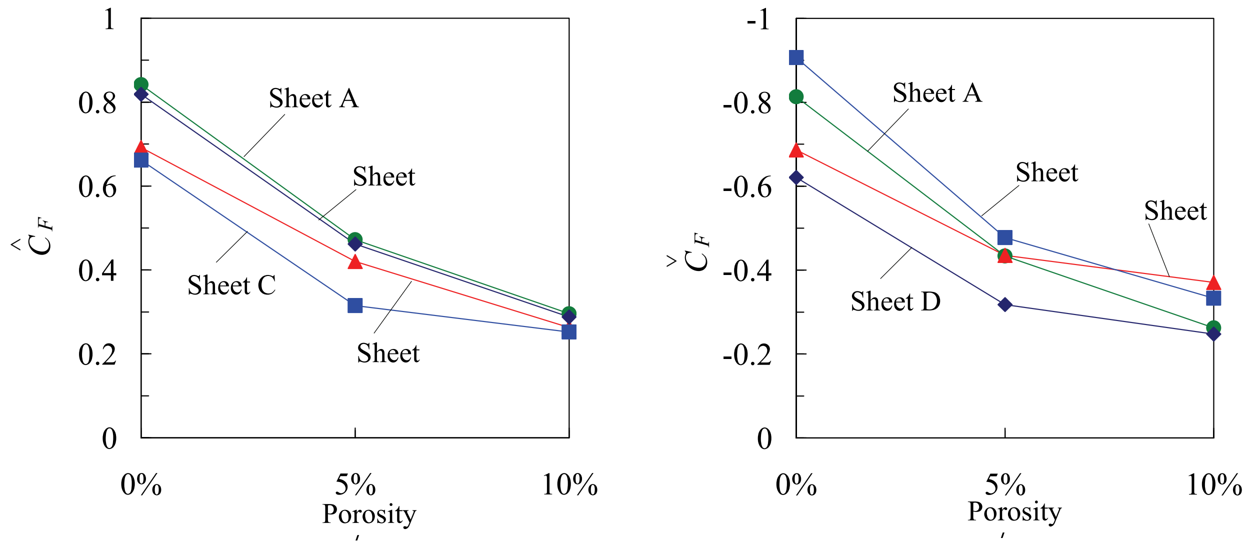

(a) Largest $\hat{C}_F$ (b) Smallest $\check{C}_F$

Fig 24: Variations of largest $\hat{C}_F$ and smallest $\check{C}_F$ with different porosities ϕ

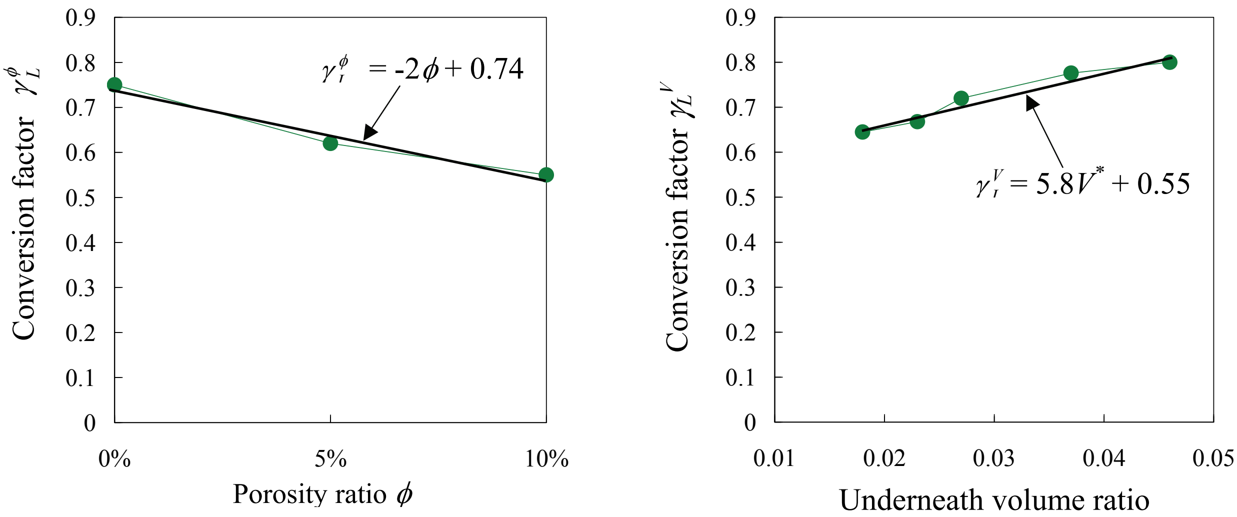

(a) Porosity ratio (b) Underneath volume

Fig 25: Variation of conversion factor

8 EVALUATION OF WIND RESISTANT PERFORMANCE OF GREEN ROOFING SYSTEM

8.1 Introduction of this research topic

With trends of increasing urban sprawl, air pollution, heat related illness and mortality, water temperatures in streams, and greenhouse gas emissions, new mitigation methods are being developed to help address these issues. One such method of mitigation is green roofing systems. Although green roofing systems are widely popular and well established in European countries, they are gaining foothold in Asia-Pacific areas such as North America, Japan and China, which can be reflected from the statistics of the new areas of green roof constructions (Year: 2000~2008) by Ministry of Land, Infrastructure, Transport and Tourism of Japan.

Although green roof systems are gaining popularity, there are few credible guidelines or requirements governing the design and application of green roof systems. During the 2006/2007 code change cycle for the International Building Code requirements, the following section was added (International Building Code, 2012):"*Section 1507.16 Roof gardens and landscaped roofs. Roof gardens and landscaped roofs shall comply with the requirements of this chapter and Sections 1607.12.3 and 1607.12.3.1 and the International Fire Code.*" As a result, green roofing systems need to be evaluated for wind resistance.

Corresponding to two types of wind-induced failures for green roofing systems, the two main objectives of this research are to investigate wind load characteristics of (1) rooftop green roof modular systems for extensive green roofing systems and (2) rooftop trees for intensive green roofing systems through wind tunnel experiments.

8.2 Characteristics of wind pressures acting on the multi-level roof

Multi-level flat roofs are widely used in building structures such as public multi-storied buildings, large scale apartments, and industrial buildings. The main concern in the structural design of these buildings was snow drift (Taylor, 1987) rather than wind loads. However, wind pressure is an important issue in roof cladding design. Moreover, rooftop energy-saving systems such as green roofing systems are becoming more and more popular and flat roofs as well as multi-level flat ones provide excellent places for such systems. In order to evaluate the wind resistant performance of such rooftop systems, wind pressure characteristics of multi-level flat roofs with different geometries need to be examined.[10]

The height of the prototype building was 30m and the building comprised of 9 stories of 3.3m in height. The geometrical scale of 1:67 was selected to accommodate future study on small-sized rooftop systems and the blockage ratio limitation (5%).

In order to conveniently change the geometry of the flat roof, the "Rubic cube" configuration was borrowed and the whole model was constructed from a combination of two kinds of plexiglass blocks. The lower part included 18 cubic blocks and the upper part comprised 27 cuboid blocks. Flat roofs with multi-level steps could thus be easily realized by removing one or several layers of upper blocks. Overall, seven types of roof configurations with different step geometries were investigated, as shown in Fig 26.

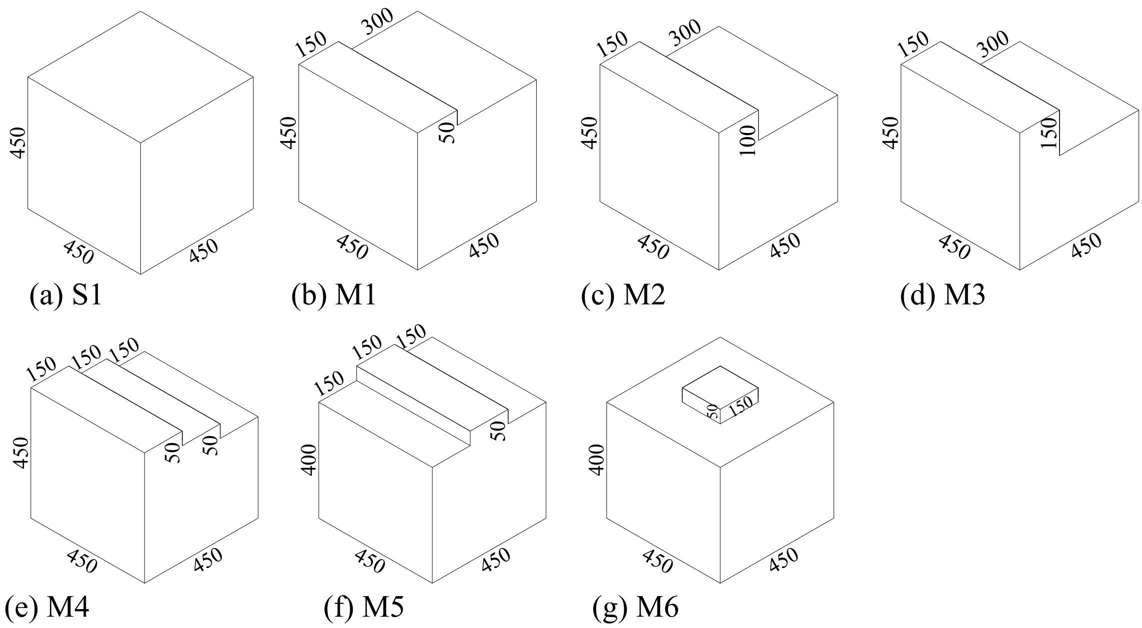

Fig 26: Experimental model

Besides the maximum (minimum) pressures among all the pressure taps for each wind direction, the structural designers are interested in the maximum (minimum) pressures among all the wind directions for each pressure tap which provide the most unfavorable values at each location.

Maximum positive and minimum negative pressure distributions among all the wind directions for a two-level roof (M1 - see Fig 26) are shown in Fig 27, and results for a simple flat roof (S1 - see Fig 26) and a three-level roof (M4 - see Fig 26) with two steps with the same total heights as the two-level roof (M1 - see Fig 26) are also given for comparison.

The smallest negative peak pressure coefficient for the two-level roof was recorded at the corner of the high-roof section and is comparable in magnitude with that for the simple flat roof. High suction pressure coefficients were also seen at both the outer and inner corners of the low roof section, which were a little smaller than those for the high roof section. For the three-level roof, the smallest negative peak pressure coefficient recorded on the high roof section was also similar to the values for the simple flat roof and the two-level roof. The most unfavourable value in the corners of the lower two roof sections was smaller than those for the two-level roof.

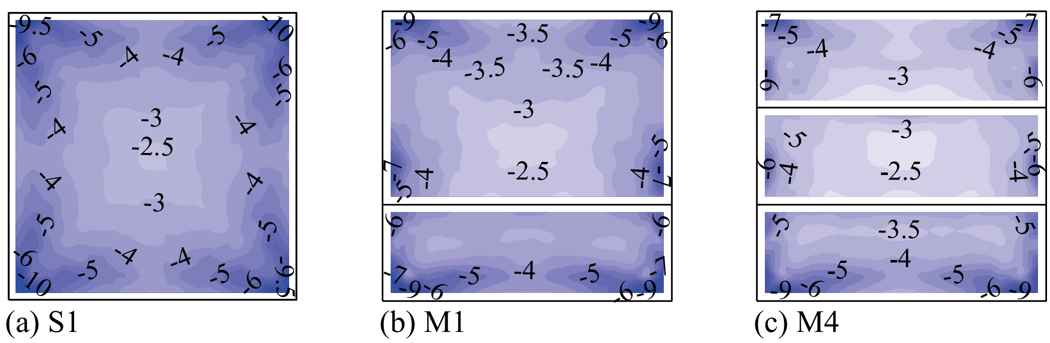

Fig 27: Minimum pressure distributions among all the wind directions

8.3 Aerodynamic characteristics of green roof modules

In order to justify the design of scaled green roof module models for a scaled wind tunnel experiment, this study was carried out to determine the characteristics of wind forces on green roof modules under uniform steady wind conditions using real green roof modules. The objectives of the present study were (a) to investigate the mean drag and uplift coefficients of real green roof modules in uniform turbulent flows, and (b) (more importantly) to verify the assumption that the effect of reconfiguration of vegetation on the wind force coefficients of green roof modules is limited. In the experiment, a total of four modules were tested, as shown in Fig 28. M0 (Fig 28(a)) is the original green roof module product of VUS500 with a plastic tray, while M2 (Fig 28(c)) and M3 (Fig 28(d)) are 1/4 part of an original green roof module product of FD-GCU II. The 1/4 parts were used because of the large weights of the full modules. A square wooden tray the same height as the original tray was used to contain the 1/4 part of growth media and vegetation. For comparison, M1, 1/4 part of the original green roof module product of VUS500, was also tested (Fig 28(b)). The coverage of the experimental modules was almost 100% and no growth media or vegetation loss occurred during the experiment.

(a) M0

(b) M1

(c) M2

(d) M3

Fig 28 Experimental specimen

Drag force coefficient which normalizes drag by the frontal area of the module A_{D2} (including tray and vegetation), considers the discrepancy in the area of exposed vegetation for each module. Therefore, the discrepancy in the values of C_{D2} is not due to the absolute amount of vegetation, but to the aerodynamic characteristics of vegetation such as permeability and flexibility. It is found that the value of C_{D2} of module M1 is still the smallest of all the tested modules, 0.6, which is similar to the value of C_{D1} for the tray. Although the type and exposed area of vegetation are different for M2 and M3 as mentioned above, the values of C_{D2} of these two modules are both close to 0.8, which is the largest value among all the tested modules. The value for M0, which adopts a commercial tray with a different size from the tray for M1~3, is 0.7, which is larger than that for M1, although the types of vegetation for M0 and M1 are the same.

The mean uplift coefficients for each module including the result for the tray plotted in a single point. It is interesting that the discrepancies among uplift force coefficients for all the modules are like a mirror of those depicted in Fig 29(b): the smallest C_V value occurs for M2 and

M3, whose C_{D2} value is the largest; the C_V value for M1 is the largest while its C_{D2} value is the lowest; and M0, whose C_{D2} value is intermediate, has a C_V value between those for M1 and M2, 3.

For comparison with the values for the tray, the M2 and M3 values are smaller while the M1 value is larger, which indicates that although the uplift coefficient for a green roof module with high vegetation tends to be smaller than that for a module with a solid square shape, there is also a possibility that the value for the module with low vegetation exceeds that for a solid module without vegetation.

The mean uplift coefficients for the modules are between 0.1 and 0.4 in the uniform wind flow condition. It is expected that, in the rooftop wind field where the uplift wind pressure is significant, the uplift force coefficient for the rooftop module will be higher than the present values.

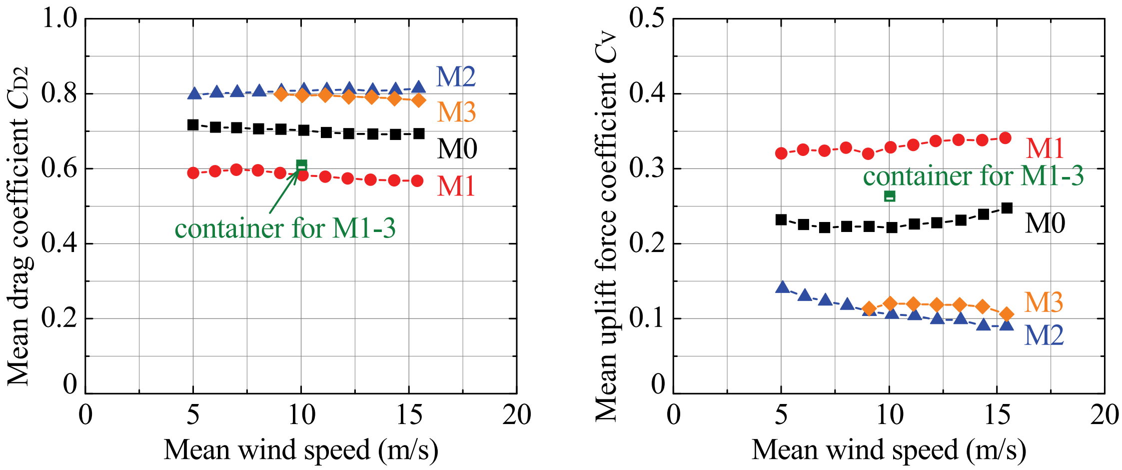

(a) Drag force coefficient (b) Uplift force coefficient

Fig 29: Force coefficient acting on real green module

8.4 Aerodynamic characteristics of green roofing tree system

The goal of this study was to evaluate the effect of wind on aerodynamic characteristics of three different tree species, including drag and overturning moment coefficients, reconfigurations and deflections. Drag coefficients based on frontal areas in still air and wind-speed-specific frontal areas were both determined; Overturning moment coefficients based on frontal areas in still air and aerodynamic centers were provided. Other parameters considered were crown porosity as affected by crown pruning, turbulence intensity and view angle.

Results of overturning moment coefficients calculated based on frontal area in still air and relative height of the aerodynamic center are shown in Figs 30 and 31, respectively. The relationships between overturning moment coefficients and wind speeds for the three species were similar to the results for drag coefficients.[11]

(a) Rose of Sharon (HS) (b) Emerald Cedar (TO) (c) Japanese Holly (IC)

Fig 30 Experimental trees

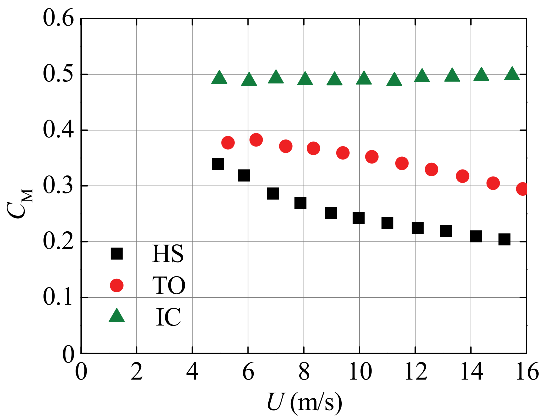

Fig 31 Variation of mean overturning moment coefficient (C_M) with wind speed (U)

This study also aimed to identify wind force characteristics of a rooftop model tree installed on a medium-rise flat-roof building in a simulated boundary layer flow, focusing on the effects of tree location, wind direction, tree crown shape and parapet height. Wind force measurements on the rooftop model tree were performed using a commercial one-component small-range force sensor for the uplift force component and a self-constructed strain-gauged force balance for the other five components. Before the experiment under rooftop conditions, 15 trial tree models of various materials, shapes and crown porosities were tested in the wind speed range from 5 m/s to 10 m/s in a smooth uniform flow. The parameters of the trial model trees were verified by comparing their drag coefficients to those for real trees described in the previous chapter.

Totally 15 trial model trees were fabricated with crowns made of porous foam, land sponge (see Fig 32) and nylon. For the crown material of porous foam and land sponge, different crown shapes were adopted: conical, cylindrical and rectangular prism for porous foam crowns, two shapes attempting to simulate a coniferous tree (Fig 32a~c) and a ball-shaped evergreen tree (Fig 32d~f) for the land sponge crowns. Three shapes for porous foam crowns were almost regular geometric, achieved by trimming the foam, while two shapes for land sponge crowns were relatively random. The trunks for the porous foam crowns were the simplest: a stainless bar with a screw thread at the bottom for connecting to the force measurement equipment, while bendable and paintable, lead-free copper armatures common in model railway scenery accessories needed to added and twisted onto the stainless bar to hold the crown materials for the land sponge and nylon crowns.

About along wind force coefficient shown in Fig.33, for case 1, the model tree was moved along the windward edge of the roof when wind was normal to the windward surface. The maximum mean and peak force coefficients occurred at the two corners and decreased from the corner to the center of the edge. The maximum mean and positive peak force coefficients were 1.3 and 3.0, respectively. For case 2, the model tree was moved along the central line of the roof along the wind direction. The maximum mean and peak force coefficients were recorded at the first location, which was nearest to the roof edge, and the values gradually decreased with distance between the model tree and the windward edge, changing from 0.1 to 0.4, and then slightly increased up to the leeward edge.

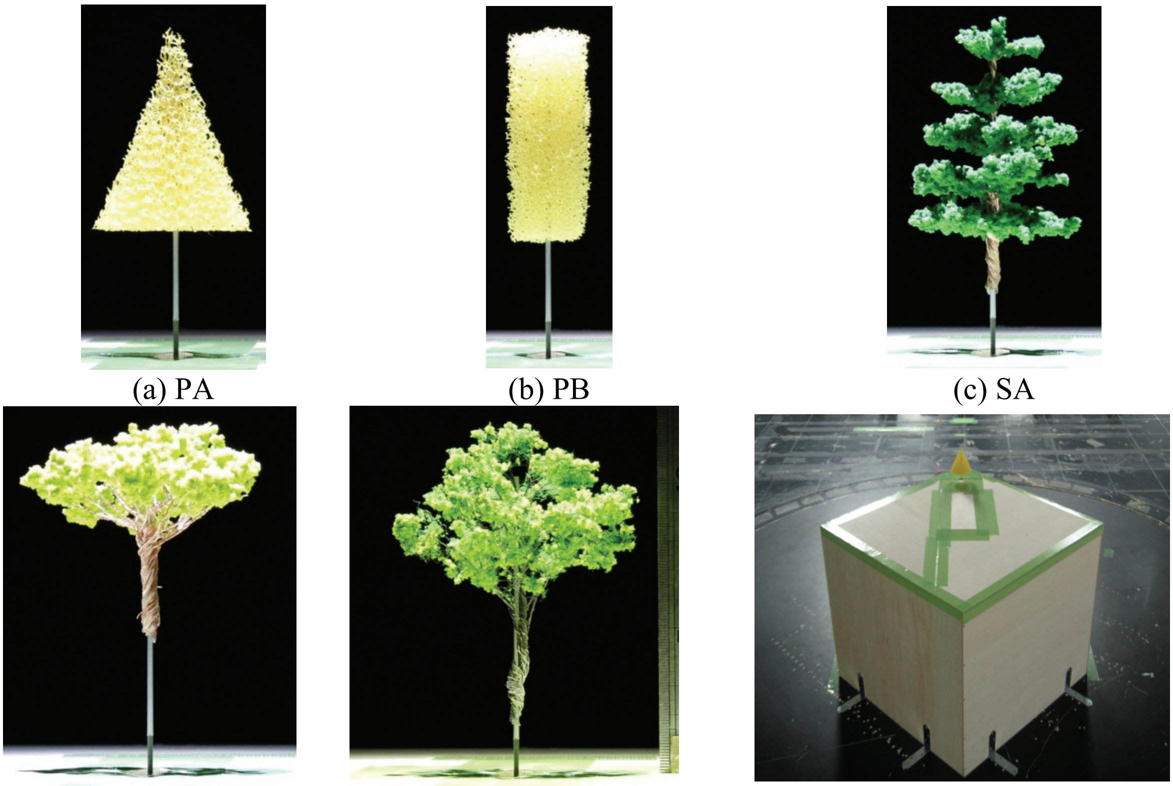

(a) PA (b) PB (c) SA

(d) SB (e) N1 (f) Setup of the rooftop model tree

Fig 32 Model trees for wind force experiment

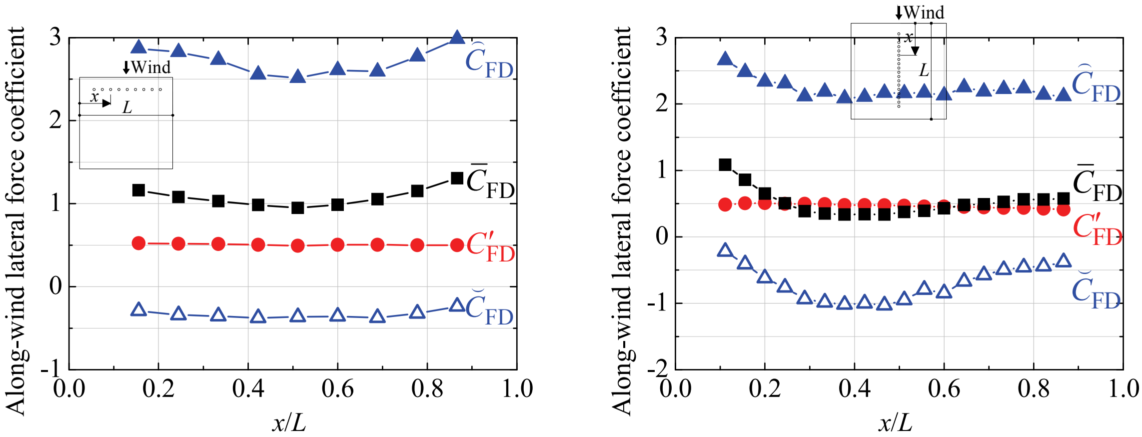

(a) Case 1 (b) Case 2

Fig 33: Along-wind lateral force coefficients on the rooftop model tree at different locations

9 CONTRIBUTIONS OF OVERALL AND LOCAL BEHAVIORS FOR LARGEST WIND LOAD EFFECTS ON STRUCTURAL MEMBERS

9.1 Introduction of this research topic

In most standards or codes for wind loads (Architectural Institute of Japan, 2004; ASCE7-05, 2005), design wind load is divided into two parts: that on structural frames based on overall structural behavior and that on components/claddings based on the local behavior of structural members. However, it is impossible to distinguish between the structural frame and components/claddings for Monocoque structures, which support the structural load by using the object’s exterior. Wind loading effects on the exterior walls depend not only on the overall bearing behavior but also on the local behavior of the shells. Current codes do not provide a means for determining the equivalent static wind load aimed at maximum loading effects for members of such structures.

The present work aimed at better understanding of wind loading effects on exterior walls of Monocoque structures. The internal stresses in the wall members were investigated by conducting time-history analysis using the finite element (FE) method, with special attention to the largest wind loading effects, including negative and positive peak member stresses. A method was proposed for estimating the contributions to the largest wind loading effects due to overall structural behavior.[12]

9.2 Wind tunnel experiment

9.2.1 *Experimental arrangements and procedures*

Wind tunnel tests were conducted at the Tokyo Polytechnic University in Japan to measure the fluctuating wind pressures. A cylindrical model 0.48m in height and 0.06m in diameter was used, with 1/250 geometric scale, as shown in Fig 34. 160 wind pressure measurement points were arranged on the exterior of the model, 16 at each level at 22.5^{o} intervals. The power exponent of the vertical profile of mean wind speed was 0.18. The mean wind speed and the turbulence intensity at the height of the model were 9.9m/s and 11%, respectively. Measured longitudinal mean wind velocity and turbulence intensity profiles are shown in Fig 35.

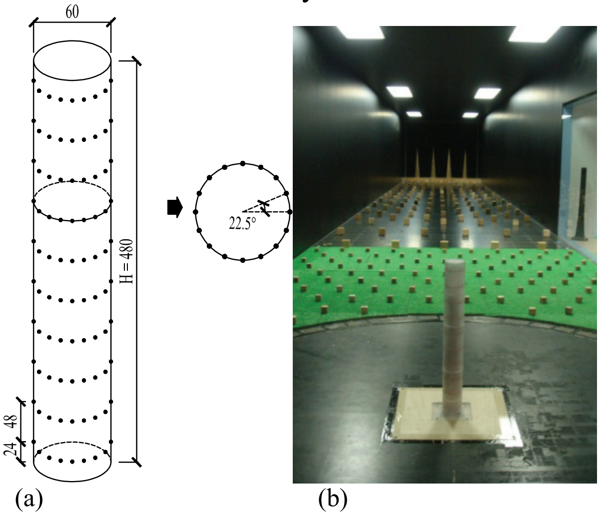

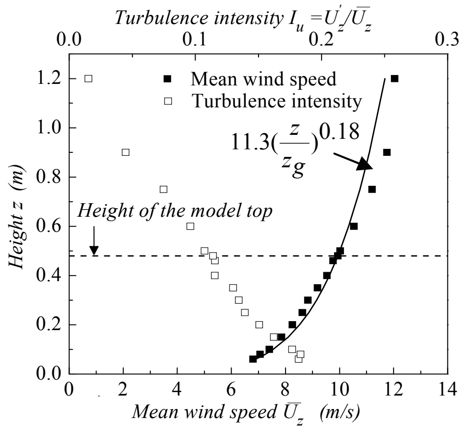

Fig 34. Wind pressure test model: (a) configuration of test model (unit: mm); (b) model in wind tunnel

Fig 35. Mean wind speed and turbulence intensity profiles

9.2.2 *Expanding fluctuating wind pressures*

Because the locations of the nodes of the FE model did not coincide with those of the pressure taps on the experimental model, the fluctuating wind pressures at the nodes were simulated by using a proper orthogonal decomposition (POD) technique. A detailed discussion of this technique is presented in Tamura et al. (1997, 1999), for example. Table 2 gives the results of the normalized eigenvalues obtained from the POD analysis. The cumulative contribution up to the 50th mode is approximately 95%. Therefore, during the following analysis, the wind pressures at the nodes were simulated for the first 50 eigen-modes.

Table 2. Contribution of each mode from POD for Monocoque model

Mode	Contribution (%)	Cumulative Contribution
1st	28.21	28.21
2nd	8.61	36.82
3rd	7.30	44.12
…	…	…
20th	0.71	85.58
50th	0.16	94.79

9.3 Numerical analysis of wind loading effects

9.3.1 *Analytical model*

The prototype structure was a steel structure. ANSYS software was used for the FE modeling and analysis. The model was clamped at the bottom end while its top end was free. According to the geometric scale in the wind tunnel, 1:250, the height and the outside diameter were 120m and 15m, respectively, with a height-to-radius aspect ratio H/R= 16. The shell wall thickness, t=12mm, was set uniform with height. The mean wind speed at the top (H=120m) was set at 50m/s. The critical damping ratios for the first and second modes were set to 1% to calculate the two coefficients for the Raleigh damping equation. In the present study, the effects of aerodynamic damping and stiffness were not considered.

9.3.2 *Estimating effects of overall behavior on member stresses*

Firstly, the fluctuating wind pressures generated by POD were directly applied to the FE model and the dynamic wind load effects due to both overall and local behaviors were obtained. Then the tip time-history displacements obtained from a 10-lumped mass model system (Fig 37) under the overall fluctuating wind forces (Fig 36), assumed to represent the overall behavior of the structure, were applied to the FE model and the load effects were calculated considering only overall behavior. The effects of the overall behaviors on the member stresses were investigated by comparisons of the stress results from the above two round time-domain analyses. It was assumed that there was no distortion on the cross sections when only overall behaviors were considered. The horizontal and rotational angular displacements of the lumped-mass system were transferred to the corresponding displacements of the nodes in the FE model.

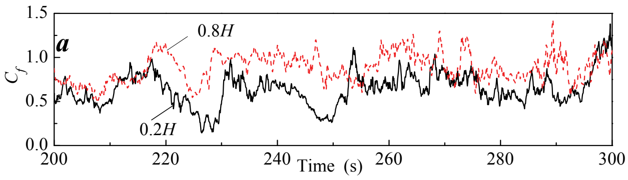

(a) along-wind

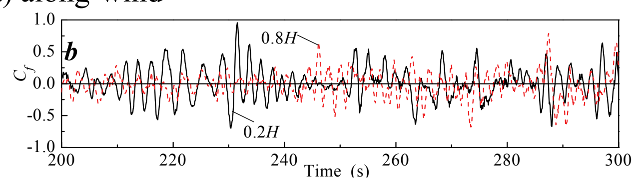

(b) across-wind

Fig 36. Overall wind force coefficients

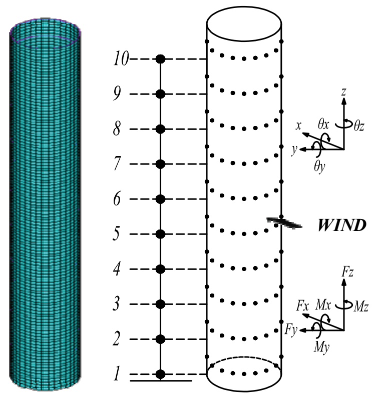

Fig 37. FE model and lumped-mass model system

9.3.3 *Results and discussions*

In the FE analysis, the global axes x, y, z were consistent with the axes defined earlier in Fig 37. In this case, σ_z represented the normal stress in the shell structure along the cylindrical axis, σ_y represented the stress in the circumferential direction and τ_{yz} represented the in-plane shear stress in the shell structure. The area located at height 0.15H to 0.25H, at angles φ, -50°~50° from the windward meridian was chosen for discussion of the stress results. There were a total of 140 shell elements in this area.

The stresses in the elements became smaller when considering the overall behavior only, especially for the circumferential stress component. Because in this case only the bending behavior of the whole shell wall was considered, the bending moment and shear force were the main internal forces. Thus, the axial and shear stresses were the predominant loading effects when considering only the overall behaviors.

The other two stress components σ_y and τ_{yz} were smaller than the axial normal stress σ_z. Fig 38 shows the maximum axial tensile stresses and axial compression stresses separately in the order of the values. It can be clearly seen that considering only the overall behavior will underestimate the loading effects on the structural members. The effects of the overall behaviors on the member stresses are estimated by calculating the ratio between the largest wind load effects, $R_{max,\, over-}$

$_{all}$/ $R_{max,\ real}$ and $R_{min,\ overall}$/ $R_{min,\ real}$. Here, $R_{max,\ overall}$ and $R_{min,\ overall}$ represent the maximum and minimum stresses under fluctuating wind load considering only overall behaviors for one element; $R_{max,\ real}$ and $R_{min,\ real}$ represent the maximum and minimum stresses under fluctuating wind load considering both overall behaviors and local behaviors. The ratios of the maximum axial normal stresses were about 65%~100%, while the ratios of the minimum axial normal stresses were about 60%~90%.

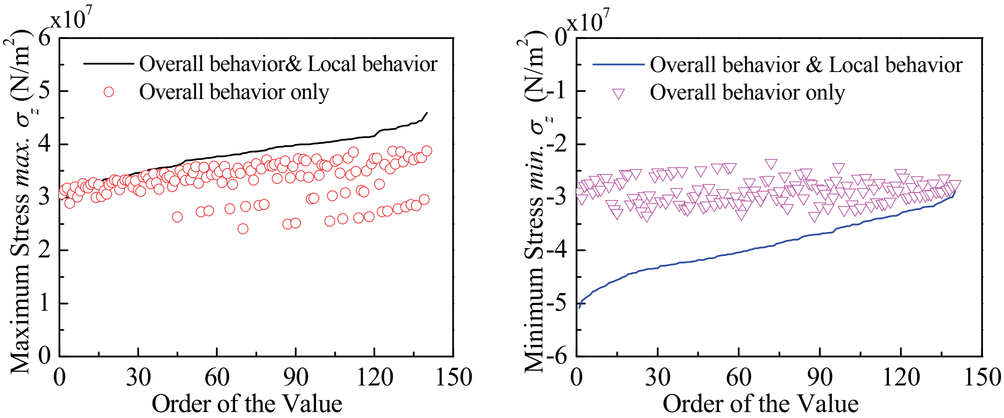

Fig 38. Comparison of maximum and minimum axial normal stresses according to order of values

9.4 Conclusion

Time-history displacements based on the overall behaviors and reconstructed fluctuating wind pressures were applied on to an FE model of a Monocoque structure. Considering only the overall behavior will underestimate the loading effects on the structural members, especially the circumferential stress component. The effects of the overall behaviors on the member stresses can be estimated by calculating the ratio between the largest wind load effects. For the elements chosen for discussion, the ratios of maximum axial normal stresses were about 65%~100%, while the ratios of minimum axial normal stresses were about 60%~90%. The error was more significant when the structural member was near the unfavorable area, where the member stresses were larger than others.

10 EVALUATION OF AMPLITUDE DEPENDENCY OF DAMPING IN BUILDINGS BASED ON STICK-SLIP CONTACT SURFACE MODEL

10.1 Introduction of this research topic

Damping has been widely thought to increase with amplitude starting from a low-amplitude limit until a high-amplitude point where the damping starts to plateau. But, such conclusions have been made based on experiments under relatively very low amplitudes. Damping appears to decrease instead of plateau with amplitude at the high-amplitude point based on experiments under relatively higher amplitudes.[13][14]

10.2 *Method to evaluate the amplitude dependency of damping*

This research aims to perform numerical and physical experiments to arrive at generalized conclusions on characteristics of damping amplitude dependency due to stick-slip surfaces (SSS) between main structural frames and secondary structural and non-structural elements, and to some extent, due to soil-structure interaction (SSI).

The numerical experiment first considers a simple 1-degree-of-freedom system with the stick-slip contact surface model defined by parameters following a force-displacement relationship similar to an elastic-perfectly-plastic (EPP) material. Cases with one SSS are studied first to gain a basic understanding of the parameters affecting their individual damping contributions. Cases with multiple SSS, with parameters of different levels of variability and considering different probability distributions, are studied next. From these numerical experiments, theoretical expressions can then be derived.

10.3 *Results and discussions*

The research work has so far completed analysis of more than 800 cases, a sample result from which is shown in Fig 39, where clearly, the damping due to SSS are shown to decrease with amplitude after a certain point.

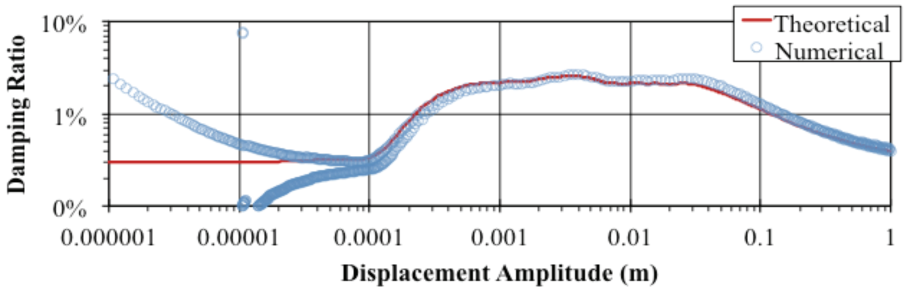

Fig 39 Sample theoretical and numerical amplitude-dependency for case with 441 SSS, and coefficient of variation = 200% and 367% for stiffness and displacement parameters, respec-

Additionally, the following general theoretical equation to characterize amplitude-dependent damping has been derived:

$$\zeta_s = \zeta_b + \frac{2}{\pi}\frac{d_{c,\mathrm{mean}}}{X}\sum_{i=1}^{N}\left(\frac{1}{1+{}^{k_b}\!/_{k_{0,\mathrm{mean}}\beta_i}\;{}^{X}\!/_{d_{c,\mathrm{mean}}\rho_i}}\right)\left(\rho_i - \frac{d_{c,\mathrm{mean}}}{X}\rho_i^2\right)\mathrm{H}\left(1-\frac{d_{c,\mathrm{mean}}}{X}\rho_i\right)$$

where ζ are the damping parameters, X is the displacement amplitude, d is the displacement parameter, k are the stiffness parameters, β and ρ are distribution parameters, and H is the Heaviside step function.

11 ESTIMETION OF STIFFNESS OF LOW-RISE STEEL HOUSE

11.1 *Introduction of this research topic*[14]

This research has focused on dynamic properties and stiffness assessment of buildings during construction. Two three-storey buildings and a one-storey experimental building model have been built for investigation. Various vibration tests includes the ambient testing, sweep testing, free vibration testing, white noise testing and earthquake excitation testing have been implemented. Amplitudes of excitation and response have been set for relatively small amplitude, medium amplitude and large amplitude levels. Effects of erection cases of buildings, structural and nonstructural components, vibration test and excitation amplitudes on dynamic properties of buildings during construction have been studied. Stiffness evaluation of buildings during construction has been investigated. FE models of full-scale three-storey buildings and experimental building model during their construction have been developed. Output-only and input-output modal identification techniques have been applied for both ambient vibration data and forced vibration data. Outline of research results are follows:

- Natural frequencies and damping ratios have been estimated for all full-scale three-storey buildings and experimental building model.
- Influences of nonstructural and structural components on dynamic properties of three-storey steel building and experimental building model have been investigated.
- 3D FE models of full-scale three-storey steel building and experimental building model during construction have been built up.
- Stiffness evaluation of experimental building during construction has been investigated.

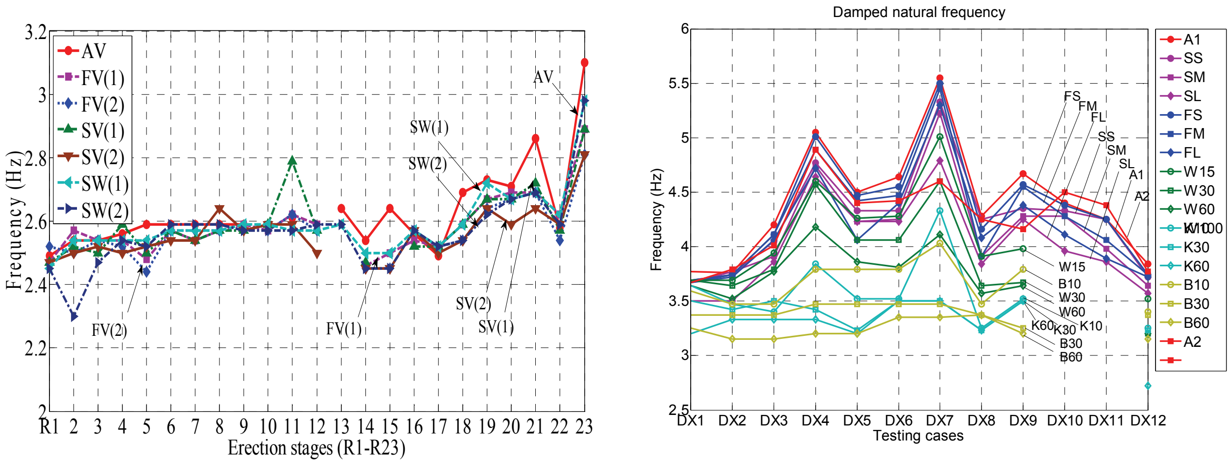

Fig 40: Dynamic properties identification and stiffness assessment

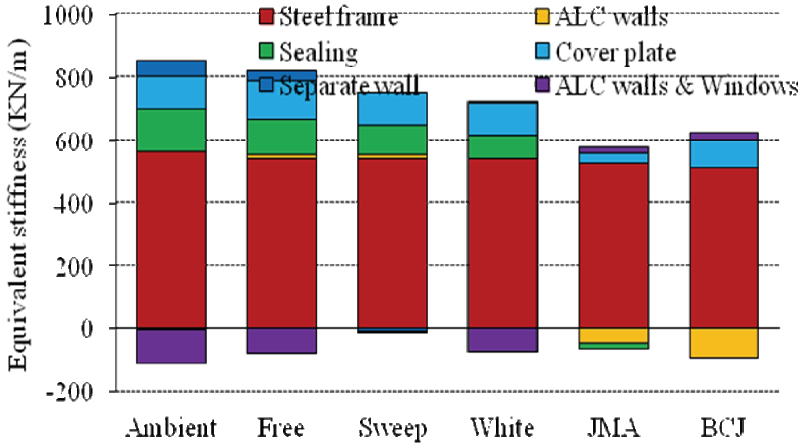

Fig 41: Estimated stiffness of secondary member

12 AERODYNAMIC CHARACTERISTICS OF VARIOUS CROSS SECTIONAL SHAPE TALL BUILDINGS WITH VARIOUS HELICAL ANGLES

12.1 Introduction of this research topic

Tall buildings are particularly prone to dynamic excitations such as those from natural disasters like strong winds and earthquakes, and this has become an especially important design issue with manhattanization. One way to minimize wind-induced vibrations of tall buildings is to focus more on their shapes in the design stage. Tanaka et.al (2012) investigated aerodynamic forces and wind pressures acting on tall buildings with various unconventional configurations. Hayashida et.al (1990) studied the effects of building plan shape on aerodynamic forces, and displacement responses have been studied for super-high-rise buildings with square and triangular cross-sections with corner modifications. Kim et.al (2002) discussed aerodynamic modifications of building shape, such as by changing the cross-section with height through tapering, which alters the flow pattern around tall buildings, and can reduce wind-induced excitations. Many researchers have tested wind pressures on buildings with irregular plans (Amin et.al., 2008), with plan shapes that change with height (Harikrishna et.al., 2009), with different rectangular cross-sections (Lin et.al., 2005), and with tapers with taper ratios of 5% and 10%, and with set-back at mid-height (Kim et.al., 2010a, 2010b, 2011). However, there have been very few studies on the aerodynamic characteristics of triangular-cross-section tall buildings with various configurations.[15]

12.2 Wind tunnel experiment

Wind tunnel tests were conducted in a boundary layer wind tunnel at the Wind Engineering Research Center, Tokyo Polytechnic University, Japan. The wind tunnel test section was 19m long with a cross-section 2.2m wide by 1.8m high. Equilateral triangle models with a side dimension of 0.076m and a height of 0.4m were used. All the models had the same volume, and Straight Triangle, Corner cut, Clover, 60°Helical, 180°Helical and 360°Helical models were tested to identify their aerodynamic characteristics. These models are shown in Fig. 42.

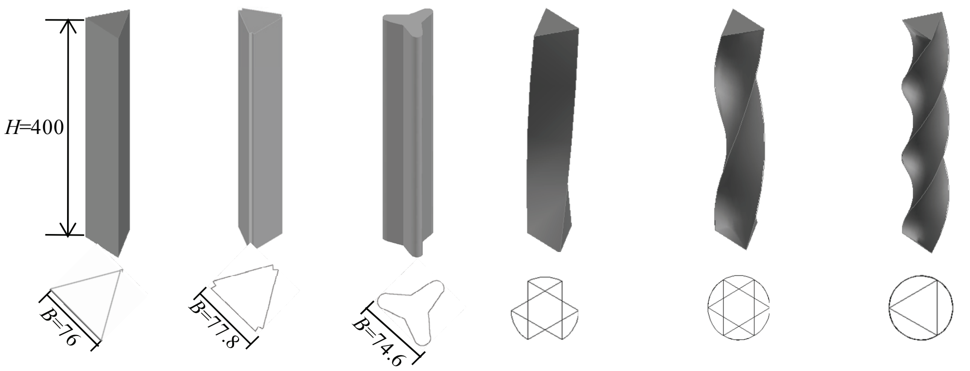

(a)Straight Triangle (b)Corner cut (c)Clover (d)60°Helical (e)180°Helical (f)360°Helical

Fig. 42. Schematic diagram of models (Unit: mm, Volume is same($1\text{x}10^6$ mm^3))

Fig. 43. shows the variation of mean along-wind OTM coefficient ($\overline{C}_{MD}$) and mean crosswind OTM coefficient($\overline{C}_{ML}$) with wind direction (θ). $\overline{C}_{MD}$ values decrease and $\overline{C}_{ML}$ values increase

as helical angle increases. The $\overline{C}_{MD}$ and $\overline{C}_{ML}$ values of the Corner cut model follow the same trend as the Straight Triangle model. The maximum and minimum values of $\overline{C}_{MD}$ are 0.64 and 0.3 for the Straight Triangle and Corner cut models. The maximum and minimum values of $\overline{C}_{ML}$ are 0.45 and -0.45 for the Straight Triangle model. For the 360° Helical model, the $\overline{C}_{ML}$ values are around 0.05~0.1 for all wind directions. The $\overline{C}_{ML}$ and $\overline{C}_{MD}$ values (around 0.1 and 0.4) for all the wind directions are almost constant for the 360°Helical model, as can be seen in Fig. 43. For the Straight Triangle model, the minimum $\overline{C}_{MD}$ occurred at 60° wind direction and the curve is 'U'-shaped. Torsional moment coefficients are not discussed here in detail as these values were very small compared to the along-wind and crosswind force coefficients. They are almost 0 for the Straight Triangle, Corner cut and Clover models. The variation of mean drag and mean lift force coefficients were 1.2 and 0 for the Straight Triangle model at 0° wind direction, which is similar to the results of Kanda et.al (1992).

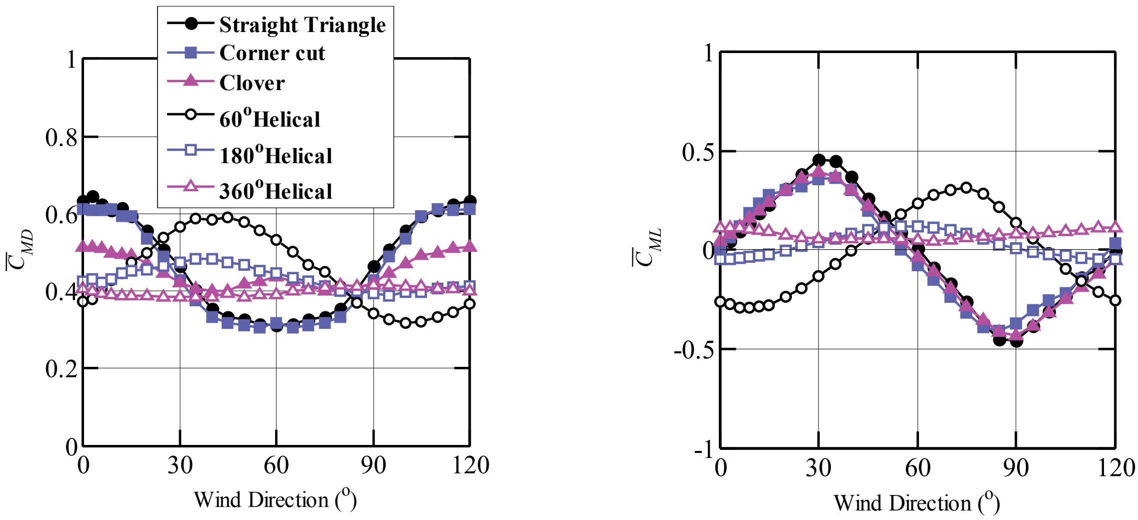

(a) Along-wind direction (b) Crosswind direction

Fig. 43. Variation of mean OTM coefficients

Fig. 44(a) shows the crosswind power spectra, fSCML, for the wind directions at which the maximum peak occurred. The maximum peaks occurred for crosswind spectra at θ=0o, 0o, 15o 45o, 120o and 30o for the Straight Triangle, Corner cut, Clover, 60oHelical, 180oHelical and 360oHelical models. A sharp peak of crosswind spectrum is observed for the Straight Triangle, Corner cut and Clover models, but the maximum peak is observed for the Clover model. The sharp peak is reduced drastically for the Helical models as the helical angle increases, indicating that the shedding vortices are more disturbed than in the normal condition. As the helical angle increases, the peak shifts to higher reduced frequency ranges, and also the band width of the spectrum increases. But for the Corner cut and Clover models, the peak appears sharp and shifts towards slightly higher reduced frequency ranges than the Straight Triangle model.

Fig. 44(b) compares in detail the square root of crosswind power spectra for the design wind speeds corresponding to higher spectral values at a 500-year return period (Up,500) and a 1-year return period (Up,1). Here, the first natural frequency is assumed to be f1=0.1Hz, and the design wind speeds are assumed to be Up,500=71m/s and Up,1=30m/s at model height H, respectively, in the Tokyo region. Then, the corresponding spectral values were calculated. The largest values decreased as the helical angle increased corresponding to Up,500, but the largest value is shown for the Clover model. For Up,1, the largest values become smaller than those for the Straight Triangle model. The Corner cut model shows the smallest value of all.

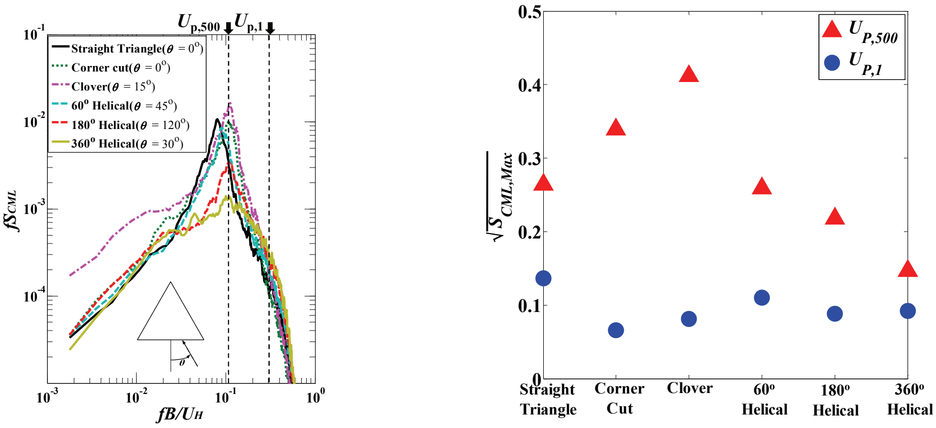

(a) Power spectral densities (b) Peak spectral values

Fig. 44. Power spectral densities of crosswind OTM coefficients and peak spectral values for 500-year and 1-year return periods

13 WIND LOAD ESTIMATION OF SOLAR ARRAY

13.1 Introduction of this research topic

The use of solar energy has extensively increased around the globe. It is therefore necessary to improve understanding of wind loading on solar collectors to ensure proper installation and to avoid damage by strong wind. In this financial year, three types of wind tunnel test were conducted for the wind loading on solar panel model with different length scale ratio. These experiments are solar panel model placed on the building model to check wind load variation for the change of building height & width, ground mounted solar panel model placed at different inclination angle & turbulent intensity and wind load reduction experiments by putting different wind blockage element.

13.2 Ground mounted solar array

The results on ground mounted solar panel model are shown in the following figures. The flow of the atmospheric boundary layer in the wind tunnel was interpreted as a geometrical model scale of 1/3.33. The layout of the solar panel model with 15º inclination angle is shown in Fig 45(a) and placed in the wind tunnel is shown in Fig 45(b). The full size was taken as 1m×2m and the model scale was 300mm×600mm. A total of 144 equally distributed pressure taps were placed on its upper and lower sides. A turbulent flow exposure area was simulated and the velocity scale was taken as 1/3.5. In this test the sampling period was 630 seconds for each sample, corresponding to 10 minutes in full scale. Mean wind force coefficient on solar panel placed at inclination angles φ = 0º, 5º, 10º, 15º, 30º and 45º for wind direction 0~180º are shown in Fig 45(c). Variation of mean wind force coefficient values at different inclination angle and its comparison with JIS C 8955:2004 are shown in Fig 45(d).

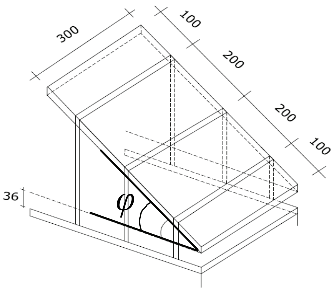

(a) Layout of solar panel model

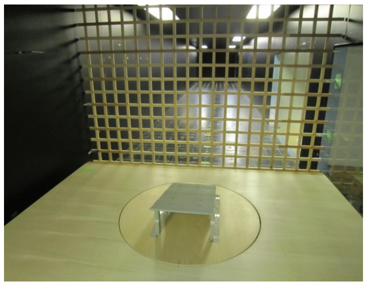

(b) Solar panel model placed in the wind tunnel

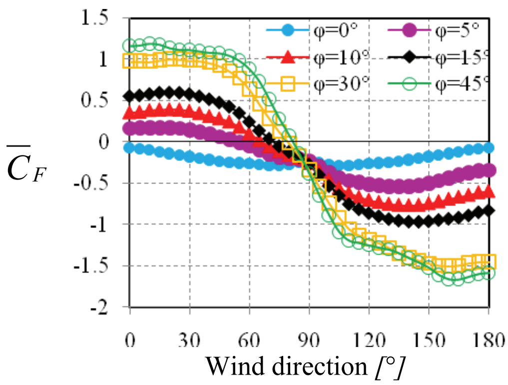

(c) Mean wind force coefficient at different inclination angle, φ

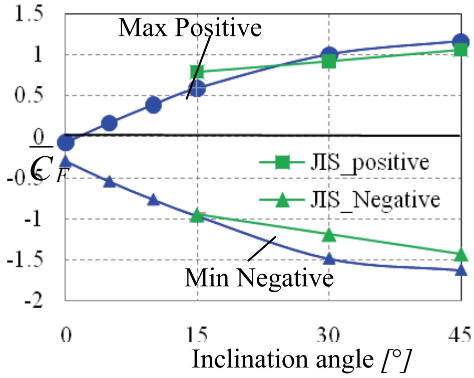

(d) Comparison of mean wind force coefficient with JIS C 8955:2004

Fig 45 Aerodynamic characteristics of ground mounted solar array

13.3 Aerodynamic characteristics of rooftop solar array [16]

A series of wind tunnel experiments have been performed to evaluate wind loads on solar panels on flat roofs, mainly focusing on module forces calculated from area-averaged net pressures on solar modules of a standard size. In order to investigate the module force characteristics at different locations on the roof, solar array models, which were fabricated with pressure taps installed as densely as possible, were moved from place to place. Design parameters including tilt angle and distance between arrays, and building parameters including building depth and parapet height, have also been considered. The results show that unfavorable negative module force coefficients for single-array cases are much larger than those for multi-array cases; tilt angle and distance between arrays increase negative module forces; effects of building depth and parapet height on negative module forces are not obvious; and recommendation values in JIS C 8955 Standard correctly estimate negative mean module force coefficients but not peak values.

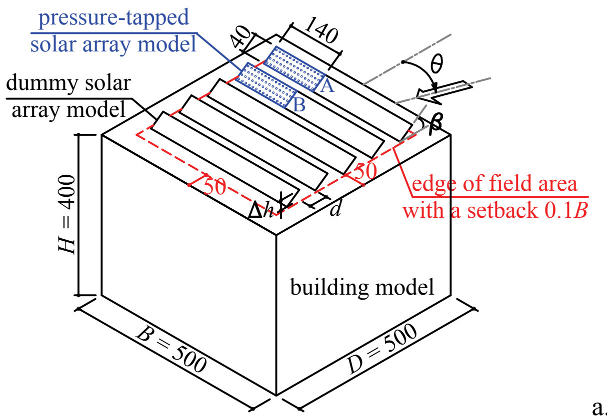

a. Experimental models

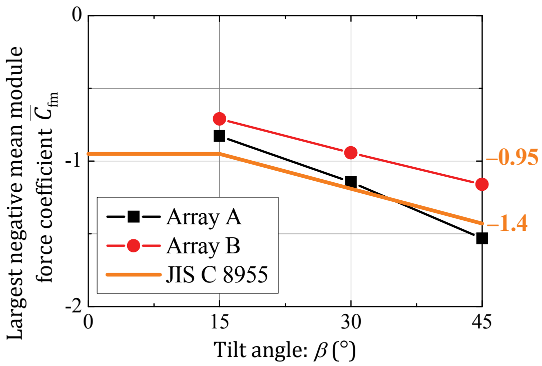

(a) Mean force coefficient

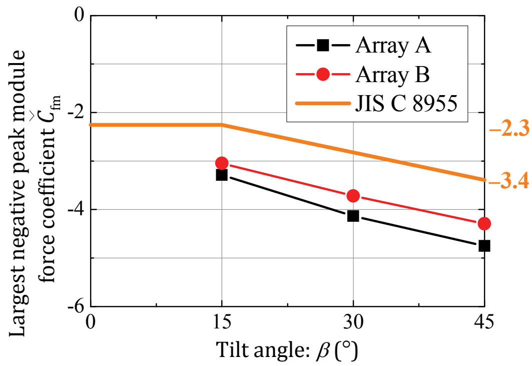

(b) Peak force coefficient

Fig 46: Effect of tilt angle on largest negative mean and peak module force coefficients

REFERENCE

[1] Sabareesh Geetha Rajasekharan, Masahiro Matsui, Yukio Tamura (2012), Characteristics of internal pressures and net local roof wind forces on a building exposed to a tornado-like vortex, Journal Wind Engineering and Industrial Aerodynamics, 112, pp.52–57

[2].Rei Okada, Masahiro Matsui, Akihito Yoshida, and Yukio Tamura (2011), Damage investigations of recent tornadoes in Japan and their publication on internet database, Rei Okada a, Masahiro Matsui, Akihito Yoshida, Yukio Tamura, Proceedings of 13th International Conference on Wind Engineering, CD-Rom, 2011.7

[3] Radhika Sudha, Yukio Tamura, Masahiro Matsui (2012), Use of post-storm images for automated tornado-borne debris path identification using texture-wavelet analysis, Journal Wind Engineering and Industrial Aerodynamics, 107-108, pp.202–213

[4] Yukio Tamura, Masahiro Matsui, L. C. Pagnini, Ryukichi Ishibashi, Akihito Yoshida, Measurement of wind-induced response of building using RTK-GPS, Journal of Wind Engineering & Industrial Aerodynamics, Vol.90, p.1783-1793, 2002.12

[5] AS/NZS 1170.2. Structural design actions, part 2: Wind actions", Australian/New Zealand Standard, 2002.

[6] Architectural Institute of Japan, AIJ Recommendations for Loads on Buildings", Architectural Institute of Japan, 2004

[7] W. Kim, Y. Tamura and A. Yoshida: Study for interference effects on local wind pressures acting on a high-rise building, Journal of the Architectural Institute of Korea, Vol. 26, No. 1, pp. 71-78,

[8] W. Kim, Y. Tamura and A. Yoshida: Interference effects of an adjacent building on local wind pressure on a high-rise building, Journal of the Architectural Institute of Korea, Vol. 26, No. 1, pp. 19-27

[9] V. T. Trung, Y. Tamura, A. Yoshida, Effects of Various Parapets on Wind Loading on Porous Sunshade Roof Cover Sheets for a Low-Rise Building, Advances in Structural Engineering, Vol. 14 No. 2 2011.02
[10] Jinxin Cao, Yukio Tamura, Akihito Yoshida, Wind pressures on multi-level flat roofs of medium-rise buildings, Journal of Wind Engineering and Industrial Aerodynamics, 103, pp.1-15, 2012
[11] Jinxin Cao, Yukio Tamura, Akihito Yoshida, Wind tunnel study on aerodynamic characteristics of shrubby specimens of three tree species, Journal of Urban Forestry & Urban Greening, 2012 (Now available in online)
[12] Zhibin Ding, Yukio Tamura, Akihito Yoshida, Contribution to member stresses due to overall wind-induced behaviors of thin-walled cylindrical shell, Journal of Wind Engineering and Industrial Aerodynamics 107-108, pp.192-201, 2012
[13] Ronwaldo E. R. Aquino, Yukio Tamura, On stick-slip phenomenon as primary mechanism behind structural damping in wind-resistant design application, Journal of Wind Engineering and Industrial Aerodynamics (Accepted for publication)
[14] Nakata, S., Le, T.H., Yoshida, A., Kiriyama, S., Naito, S., Tamura, Y. (2011), “Influence of nonstructural and structural components on dynamic properties of experimental building model on a shaker”, Engineering Structures (under review)
[15] Eswara Kumar Bandi, Yukio Tamura, Akihito Yoshida, Yong Chul Kim, Qing Shan Yang, Experimental investigation on aerodynamic characteristics of various triangular-section high-rise buildings, Journal of Wind Engineering and Industrial Aerodynamics (underreview)
[16] Jinxin Cao, Akihito Yoshida, Proshit Kumar Saha, Yukio Tamura, Wind loading characteristics of panel modules in rooftop solar arrays, Journal of Wind Engineering and Industrial Aerodynamics (underreview)